

<b>REPORT DOCUMENTATION PAGE</b>			Form Approved OMB NO. 0704-0188		
<p>The public reporting burden for this collection of information is estimated to average 1 hour per response, including the time for reviewing instructions, searching existing data sources, gathering and maintaining the data needed, and completing and reviewing the collection of information. Send comments regarding this burden estimate or any other aspect of this collection of information, including suggestions for reducing this burden, to Washington Headquarters Services, Directorate for Information Operations and Reports, 1215 Jefferson Davis Highway, Suite 1204, Arlington VA, 22202-4302. Respondents should be aware that notwithstanding any other provision of law, no person shall be subject to any penalty for failing to comply with a collection of information if it does not display a currently valid OMB control number.</p> <p>PLEASE DO NOT RETURN YOUR FORM TO THE ABOVE ADDRESS.</p>					
1. REPORT DATE (DD-MM-YYYY) 01-04-2016		2. REPORT TYPE Final Report		3. DATES COVERED (From - To) 1-May-2012 - 31-Dec-2015	
4. TITLE AND SUBTITLE Final Report: Ballistic Imaging and Scattering Measurements for Diesel Spray Combustion: Optical Development and Phenomenological Studies			5a. CONTRACT NUMBER W911NF-12-1-0166		
			5b. GRANT NUMBER		
			5c. PROGRAM ELEMENT NUMBER 611102		
6. AUTHORS Terence Parker, Jason Porter, Sean Duran			5d. PROJECT NUMBER		
			5e. TASK NUMBER		
			5f. WORK UNIT NUMBER		
7. PERFORMING ORGANIZATION NAMES AND ADDRESSES Colorado School of Mines 1500 Illinois Street, Guggenheim Hall, Room 130  Golden, CO 80401 -1887			8. PERFORMING ORGANIZATION REPORT NUMBER		
9. SPONSORING/MONITORING AGENCY NAME(S) AND ADDRESS (ES) U.S. Army Research Office P.O. Box 12211 Research Triangle Park, NC 27709-2211			10. SPONSOR/MONITOR'S ACRONYM(S) ARO		
			11. SPONSOR/MONITOR'S REPORT NUMBER(S) 61328-EG.8		
12. DISTRIBUTION AVAILABILITY STATEMENT Approved for Public Release; Distribution Unlimited					
13. SUPPLEMENTARY NOTES The views, opinions and/or findings contained in this report are those of the author(s) and should not be construed as an official Department of the Army position, policy or decision, unless so designated by other documentation.					
14. ABSTRACT Ballistic imaging using a 15 picosecond pulse laser in high-injection-pressure diesel sprays is reported. An optical Kerr effect shutter, constructed from a CS2 liquid cell and activated by a 15 picosecond pulse at 1064 nm, produces effective 532 nm imaging pulses between 7 and 15 picoseconds. The performance of the imaging system is characterized using an Air Force target positioned before an optical cell filled with polystyrene spheres in a water suspension. The impact of spatial filtering, temporal filtering, and scattering path length on image resolution are reported. The technique is demonstrated by imaging the near-critical region of methyl oleate and methyl butyrate.					
15. SUBJECT TERMS spray imaging, spray breakup, ballistic imaging, droplet scattering					
16. SECURITY CLASSIFICATION OF:			17. LIMITATION OF ABSTRACT UU	15. NUMBER OF PAGES	19a. NAME OF RESPONSIBLE PERSON Terence Parker
a. REPORT UU	b. ABSTRACT UU	c. THIS PAGE UU			19b. TELEPHONE NUMBER 303-273-3399

## Report Title

### Final Report: Ballistic Imaging and Scattering Measurements for Diesel Spray Combustion: Optical Development and Phenomenological Studies

#### ABSTRACT

Ballistic imaging using a 15 picosecond pulse laser in high-injection-pressure diesel sprays is reported. An optical Kerr effect shutter, constructed from a CS<sub>2</sub> liquid cell and activated by a 15 picosecond pulse at 1064 nm, produces effective 532 nm imaging pulses between 7 and 15 picoseconds. The performance of the imaging system is characterized using an Air Force target positioned before an optical cell filled with polystyrene spheres in a water suspension. The impact of spatial filtering, temporal filtering, and scattering path length on image resolution are reported. The technique is demonstrated by imaging the near-orifice region of methyl oleate and methyl butyrate sprays injected using a high-pressure single-hole fuel injector with direct comparison against simultaneous orthogonal shadowgraphy.

The first successful demonstration of picosecond ballistic imaging using a 15 picosecond-pulse-duration laser in diesel sprays at temperature and pressure is also reported. This technique is used to image the near-orifice region (first 3mm) of diesel sprays from a high-pressure single-hole fuel injector. Ballistic imaging of dodecane and methyl oleate sprays are reported. Ballistic images of diesel injection at pre-ignition engine-like conditions are reported. Dodecane was injected into air heated to 600°C and pressurized to 20 atm. The resulting images of the near-orifice region at these conditions reveal dramatic shedding of the liquid near the nozzle, an effect that has been predicted, but to our knowledge never before imaged. These shedding structures have an approximate spatial frequency of 10 mm<sup>-1</sup> with lengths from 50 to 200 microns. Several parameters are explored including injection pressure, liquid fuel temperature, air temperature and pressure, and fuel type. Resulting trends are summarized with accompanying images.

The frequency doubled (532nm) and tripled (355nm) output of the Nd:Yag laser were converted to pulse sheets using cylindrical lenses to acquire cross sections of the spray interior. These sheets were then aligned to pass through the spray at varying offset distances from the spray centerline. Orthogonal imaging of the scattering light sheets reveal internal spray structure not previously observed using the ballistic imaging method. Sheet scattering further revealed that an intact liquid core is not observed at the injection pressures investigated. Images indicate a droplet-laden flow with significant shear-driven vortical structures, highly transient spray breakup, and significant internal spray structure.

---

**Enter List of papers submitted or published that acknowledge ARO support from the start of the project to the date of this printing. List the papers, including journal references, in the following categories:**

**(a) Papers published in peer-reviewed journals (N/A for none)**

<u>Received</u>	<u>Paper</u>
02/27/2015 5.00	Sean P. Duran, Jason M. Porter, Terence E. Parker. Ballistic imaging of diesel sprays using a picosecond laser: characterization and demonstration, Applied Optics, (02 2015): 1743. doi: 10.1364/AO.54.001743
04/14/2015 6.00	Sean P. Duran, Jason M. Porter, Terence E. Parker. Picosecond ballistic imaging of diesel injection in high-temperature and high-pressure air, Experiments in Fluids, (04 2015): 0. doi: 10.1007/s00348-015-1953-3
<b>TOTAL:</b>	<b>2</b>

Number of Papers published in peer-reviewed journals:

---

(b) Papers published in non-peer-reviewed journals (N/A for none)

Received      Paper

TOTAL:

Number of Papers published in non peer-reviewed journals:

---

(c) Presentations

Number of Presentations: 0.00

---

Non Peer-Reviewed Conference Proceeding publications (other than abstracts):

Received      Paper

04/14/2015	7.00	Jason M. Porter, Sean P. Duran, Terence E. Parker. Picosecond Ballistic Imaging of Ligament Structures in the Near-Nozzle Region of Diesel Sprays, ILASS Americas 27th Annual Conference on Liquid Atomization and Spray Systems, Raleigh, NC, May 2015. 17-MAY-15, . : ,
09/02/2013	2.00	Sean Duran, Jason Porter, Terence Parker. Ballistic Imaging of Sprays at Diesel Relevant Conditions, ICLASS. 02-SEP-12, . : ,

TOTAL:      2

Number of Non Peer-Reviewed Conference Proceeding publications (other than abstracts):

---

Peer-Reviewed Conference Proceeding publications (other than abstracts):

Received      Paper

TOTAL:

Number of Peer-Reviewed Conference Proceeding publications (other than abstracts):

---

(d) Manuscripts

<u>Received</u>		<u>Paper</u>
01/01/2015	4.00	Sean P. Duran, Jason M. Porter, Terence E. Parker. Picosecond Ballistic Imaging of Diesel Injection in High Temperature and Pressure Air, Experiments in Fluids (12 2014)
09/02/2013	1.00	Sean Duran, Jason Porter, Terence Parker. Ballistic Imaging of a Diesel Injector Spray at High Temperature and Pressure, Experiments in Fluids (09 2013)
10/15/2014	3.00	Sean Duran, Jason Porter, Terence Parker. Ballistic Imaging of Diesel Sprays Using a Picosecond Laser: Characterization and Demonstration, Applied Optics (10 2014)
TOTAL:		3

Number of Manuscripts:

---

Books

<u>Received</u>	<u>Book</u>
TOTAL:	

<u>Received</u>	<u>Book Chapter</u>
TOTAL:	

## Patents Submitted

## Patents Awarded

## Awards

## Graduate Students

<u>NAME</u>	<u>PERCENT SUPPORTED</u>	Discipline
Sean Duran	1.00	
Jeffrey Wheeler	0.10	
<b>FTE Equivalent:</b>	<b>1.10</b>	
<b>Total Number:</b>	<b>2</b>	

## Names of Post Doctorates

<u>NAME</u>	<u>PERCENT SUPPORTED</u>
<b>FTE Equivalent:</b>	
<b>Total Number:</b>	

## Names of Faculty Supported

<u>NAME</u>	<u>PERCENT SUPPORTED</u>	National Academy Member
Jason Porter	1.00	
Terence Parker	0.00	
<b>FTE Equivalent:</b>	<b>1.00</b>	
<b>Total Number:</b>	<b>2</b>	

## Names of Under Graduate students supported

<u>NAME</u>	<u>PERCENT SUPPORTED</u>
<b>FTE Equivalent:</b>	
<b>Total Number:</b>	

### Student Metrics

This section only applies to graduating undergraduates supported by this agreement in this reporting period

The number of undergraduates funded by this agreement who graduated during this period: ..... 0.00

The number of undergraduates funded by this agreement who graduated during this period with a degree in science, mathematics, engineering, or technology fields:..... 0.00

The number of undergraduates funded by your agreement who graduated during this period and will continue to pursue a graduate or Ph.D. degree in science, mathematics, engineering, or technology fields:..... 0.00

Number of graduating undergraduates who achieved a 3.5 GPA to 4.0 (4.0 max scale):..... 0.00

Number of graduating undergraduates funded by a DoD funded Center of Excellence grant for Education, Research and Engineering:..... 0.00

The number of undergraduates funded by your agreement who graduated during this period and intend to work for the Department of Defense ..... 0.00

The number of undergraduates funded by your agreement who graduated during this period and will receive scholarships or fellowships for further studies in science, mathematics, engineering or technology fields: ..... 0.00

### Names of Personnel receiving masters degrees

NAME

**Total Number:**

### Names of personnel receiving PHDs

NAME

Sean Duran (Summer 2016)

**Total Number:**

1

### Names of other research staff

NAME

PERCENT SUPPORTED

**FTE Equivalent:**

**Total Number:**

### Sub Contractors (DD882)

### Inventions (DD882)

### Scientific Progress

See Attachment

### Technology Transfer

# **Final Report: Ballistic Imaging and Scattering Measurements for Diesel Spray Combustion: Optical Development and Phenomenological Studies**

Sean P. Duran, Jason M. Porter, Terence E. Parker

Mechanical Engineering Department  
Colorado School of Mines, Golden, CO, 80401

## **Abstract**

Ballistic imaging using a 15 picosecond pulse laser in high-injection-pressure diesel sprays is reported. An optical Kerr effect shutter, constructed from a CS<sub>2</sub> liquid cell and activated by a 15 picosecond pulse at 1064 nm, produces effective 532 nm imaging pulses between 7 and 15 picoseconds. The performance of the imaging system is characterized using an Air Force target positioned before an optical cell filled with polystyrene spheres in a water suspension. The impact of spatial filtering, temporal filtering, and scattering path length on image resolution are reported. The technique is demonstrated by imaging the near-orifice region of methyl oleate and methyl butyrate sprays injected using a high-pressure single-hole fuel injector with direct comparison against simultaneous orthogonal shadowgraphy.

The first successful demonstration of picosecond ballistic imaging using a 15 picosecond-pulse-duration laser in diesel sprays at temperature and pressure is also reported. This technique is used to image the near-orifice region (first 3mm) of diesel sprays from a high-pressure single-hole fuel injector. Ballistic imaging of dodecane and methyl oleate sprays are reported. Ballistic images of diesel injection at pre-ignition engine-like conditions are reported. Dodecane was injected into air heated to 600°C and pressurized to 20 atm. The resulting images of the near-orifice region at these conditions reveal dramatic shedding of the liquid near the nozzle, an effect that has been predicted, but to our knowledge never before imaged. These shedding structures have an approximate spatial frequency of 10 mm<sup>-1</sup> with lengths from 50 to 200 microns. Several parameters are explored including injection pressure, liquid fuel temperature, air temperature and pressure, and fuel type. Resulting trends are summarized with accompanying images.

The frequency doubled (532nm) and tripled (355nm) output of the Nd:Yag laser were converted to pulse sheets using cylindrical lenses to acquire cross sections of the spray interior. These sheets were then aligned to pass through the spray at varying offset distances from the spray centerline. Orthogonal imaging of the scattering light sheets reveal internal spray structure not previously observed using the ballistic imaging method. Sheet scattering further revealed that an intact liquid core is not observed at the injection pressures investigated. Images indicate a droplet-laden flow with significant shear-driven vortical structures, highly transient spray breakup, and significant internal spray structure.

# Table of Contents

<b>Abstract .....</b>	<b>1</b>
<b>Table of Contents.....</b>	<b>2</b>
<b>List of Figures .....</b>	<b>3</b>
<b>1. Executive Summary.....</b>	<b>6</b>
1.1 Literature review .....	6
<b>2. Ballistic Imaging Characterization .....</b>	<b>7</b>
<b>2.1 Experimental Methods.....</b>	<b>8</b>
2.2.1 Ballistic imaging optical train .....	8
2.2.2 Image capture .....	9
<b>2.3 Method Characterization.....</b>	<b>9</b>
2.3.1 Optical Kerr effect shutter.....	10
2.3.2 Temporal filtering .....	11
2.3.3 Spatial filtering .....	12
2.3.4 Overall imaging performance.....	13
<b>2.4 Conclusions .....</b>	<b>13</b>
<b>3.1 Diesel Spray Imaging .....</b>	<b>13</b>
<b>3.2 Experimental Methods.....</b>	<b>14</b>
3.2.1 Ballistic imaging optical train .....	14
3.2.2 Image processing.....	15
3.2.3 Image capture .....	15
3.2.4 Diesel injection system.....	16
3.2.5 Orthogonal imaging.....	17
<b>3.3 Diesel Spray Imaging Results &amp; Discussion.....</b>	<b>19</b>
3.3.2 Evolution of a spray .....	20
3.3.3 Effect of fuel type on spray behavior .....	21
3.3.4 Transient fluctuations in room temperature dodecane sprays .....	21
3.3.5 Injection pressure and double pulsed injection .....	22
3.3.6 Effect of charge pressure on dodecane sprays .....	22
3.3.7 Effect of charge temperature and pressure on dodecane sprays.....	23
3.3.8 Spray structure in a biodiesel surrogate .....	25
<b>3.4 Conclusions .....</b>	<b>26</b>
<b>4 Two-Color Droplet Scattering.....</b>	<b>26</b>
<b>4.1 Introduction .....</b>	<b>26</b>
<b>4.2 Experimental Methods .....</b>	<b>27</b>
<b>4.3 Results.....</b>	<b>30</b>
<b>4.2 Conclusions .....</b>	<b>37</b>
<b>5 Project Summary .....</b>	<b>38</b>
<b>6 References .....</b>	<b>38</b>



## List of Figures

Figure 1: Experimental schematic of ballistic imaging optical train for characterization experiments. A polystyrene sphere suspension and Air Force target provide a well-characterized scattering medium and image. P1-P5 are polarizers. Beams are shown cw for clarity. ....	8
Figure 2. Schematic diagram of the time overlap of the imaging beam and gate beam at the optical Kerr effect shutter. Changing this overlap in time effectively changes the “on” time for the shutter. ....	9
Figure 3. Performance of the Kerr cell as measured by autocorrelation. Image beam intensity decreases with increasing delay between the arrival of the gate and image beam at the Kerr cell (top). The ideal delay between gate and image beams yields the minimum gate width of 7 ps. The arrow indicates the timing used in these experiments. ....	10
Figure 4. Air Force target images using a 532nm switching beam (left) and a 1064 nm switching beam (right). Images collected without any scattering medium present. ....	11
Figure 5. CTF calculated from an Air Force target imaged through a 20mm cell filled with 5 $\mu$ m polystyrene spheres suspended in water (OD = 6.71). Spatial filtering was used with a solid angle of collection of $\Omega = 0.002$ sr. At 20mm, the OKE gate has a measureable effect on CTF. Data points represent the average of 3 line pairs with error bars equal to the standard deviation. ....	11
Figure 6. CTF of Air Force target images captured using 10mm scattering cell (OD = 8.35) with and without spatial filtering. Images were taken without OKE gate. ....	12
Figure 7. Highest resolution image achieved at increasing optical depth. Resolution decreases with increasing OD. Resolution was determined from the highest number of lines/mm discernable on the Air Force target. ....	13
Figure 8: Experimental schematic of ballistic imaging optical train. The HeNe laser and separate detectors are to measure the arrival of the imaging pulse and the spray injection timing. P1-P5 are polarizers. Beams are shown as cw for clarity. ....	15
Figure 9: A visual guide to the image processing steps used in capturing ballistic images of sprays. These images were collected with the Cascade camera. ....	15
Figure 10: A schematic of the electronic timing used during imaging. ....	16
Figure 11: The Diesel Engine Simulator. Air or nitrogen is preheated by packed bed of steel ball bearings. Fuel is injected into the heated chamber toward a steal plate, which simulates the top surface of a piston. ....	17
Figure 12. Optical layout for simultaneous orthogonal imaging of a fuel spray using ballistic (camera 1) and shadowgraphy (camera 2) techniques. ....	18
The complexity of the ballistic imaging optical train may raise the question of whether this type of imaging is required to study the near-orifice region of diesel sprays. To quantify improvements in image resolution and clarity, sprays were imaged simultaneously using the ballistic imaging technique, with spatial filtering (solid angle of collection of $\Omega = 0.002$ sr), and with traditional shadowgraphy. To accomplish this, the imaging beam was passed through a 50/50 beam splitter and into orthogonal optical paths (Figure 12). The Myo camera was used for the ballistic imaging line (Camera 1), while the Cascade camera was used for the shadowgraphy experiments (Camera 2). Two identical cameras were not available at the time of these experiments, so the resolution of the two images has been matched via image post processing in Matlab (Figure 13). ....	18

Figure 14: Orthogonal and simultaneous ballistic images and traditional shadowgraphs of a methyl butyrate spray (a-b) and a methyl oleate spray (c) injected at 1450 atm into ambient air. Image resolution for the ballistic image in (a) is 500 x 900 and 170 x 300 for the images in (b) and (c). The ballistic images in (b) and (c) were post processed to reduce their resolution to match the shadowgraph images. The scale of optical depth, OD, is shown in the color bar on the right. ....	18
Figure 15: Simultaneous orthogonal imaging of a methyl oleate spray injected at 1450 atm into ambient air. Image resolution for both images is 170 x 300. ....	20
Figure 16: Ballistic images of methyl butyrate sprays injected at 1450 atm into ambient air and captured at increasing times after start of injection. The total duration of a typical injection is 3 ms. The scale of optical depth, OD, is shown in the color bar on the right. ....	20
Figure 17: Comparison of ballistic images of methyl oleate and methyl butyrate sprays at 1450 atm injection pressure in ambient air. The scale of optical depth, OD, is shown in the color bar on the right. ....	21
Figure 18: Images at different times (relative to start of injection) in separate dodecane sprays. ....	22
Figure 19: Ballistic images of dodecane at various injection pressures revealed significant shedding in all cases. ....	22
Figure 20: Images of a double-pulsed sequence of injections shows similar structure in each spray. ....	22
Figure 21: (left) Images of dodecane at room temperature and increasing pressures. Magnification with additional contrasting highlights shedding phenomena. (right) Spray cone angle increased with increasing charge pressure. Data points are averages over ~30 images each. Error bars represent one standard deviation. ....	23
Figure 22: (left) Example images which exhibit the trend of increasing cone angle with pressure. (right) Averaged cone angle for all sprays studied. Data points are averages over ~30 images each. Error bars represent one standard deviation. ....	24
Figure 23: The offset distance between the shedding structures and the injector orifice varied with pressure. ....	24
Figure 24: Measured spray cone angles as a function of time. Sprays were injected into a 20 atm environment at 25° and 600°C. The smooth region of the 600°C curve corresponds to the observation of spray shedding. ....	25
Figure 25: Images of methyl oleate reveal a wider spray cone and peripheral shedding. ....	26
Figure 26: Two-sheet scattering measurement. 532nm and 355nm pulse sheets are simultaneously passed through the spray. Images of the scattering from these sheets is captured by two camera systems. ....	27
Figure 27: Experimental setup for two-color scattering measurement. Green beam (532nm), blue beam (355nm), C: camera, L: lens, I: iris, PH: laser pinhole, P: polarizer, WP: wave plate, M: mirror, CL: cylindrical lens, DM: dichroic mirror, S: spray, BD: beam dump, BP: band pass filter. ....	28
Figure 28: Dodecane spray (320 $\mu$ m injector) at 0.6 ms ASOI. ....	31
Figure 29: Scattering images of dodecane injections at 1.9 ms ASOI. Spray position moved relative to beam. Dimensions listed are offset from spray centerline, with negative values being further from the camera. ....	31
Figure 30: End of spray images (355 nm) showing effect of fuel type and orifice size. Oil was added to the tip of the injector to simulate what a liquid core would look like. ....	32
Figure 31: On centerline images of dodecane spray (160 $\mu$ m injector) with decreasing injection pressure. ....	32
Figure 32: 355nm image of spray at 0.3 ms ASOI. Typical spray features due to fuel effects and orifice size differences. ....	33

Figure 33. Dodecane injection, 160 $\mu\text{m}$ injector, with 355nm laser. Droplet vortices are present in the spray. ....	34
Figure 34. Methyl oleate (left) and dodecane (right) injected from 160 $\mu\text{m}$ orifice at 1450 atm (imaged with 355 nm wavelength). ....	35
Figure 35. Dodecane injected from 320 $\mu\text{m}$ orifice at 1450 atm (imaged with 355 nm wavelength). ....	36
Figure 36. Methyl oleate injected from 320 $\mu\text{m}$ orifice at 1450 atm (imaged with 355 nm wavelength). ....	37

## **1. Executive Summary**

This final report combines three significant pieces of work: two existing journal papers that are reproduced here more or less intact, and results from a new, yet unpublished spray study using laser sheet scattering. Two primary techniques are reported: ballistic imaging and orthogonal laser sheet scattering. These two techniques have revealed the internal structure of diesel sprays in the near-nozzle region, have shown a significant dependence on fuel type, injector type, temperature, and pressure, and demonstrated the highly transient nature of these sprays.

Understanding primary atomization in the near-orifice region of sprays remains one of the outstanding questions in multiphase flows [1]. In particular, a detailed understanding of the mechanisms driving primary atomization is vital to improved combustion efficiency in advanced combustion engines and propulsion systems [2]. Despite the importance of this research, there remains a lack of quality experimental data for validation of new models [3]. Further complicating the problem, the high injection pressures of modern combustion systems achieve Reynolds numbers that are too high for direct numerical simulation. In spite of these challenges, models are now being developed that capture primary atomization in these sprays [4], [5].

The optical methods developed here are capable of probing the high-density region of diesel sprays for improved understanding of near-orifice spray behavior (considered here to be the first ~3mm below the injector). The controlling breakup modes of diesel sprays for operating ranges relevant to diesel engines have been studied by coupling ballistic imaging (BI) with the well-controlled, diesel-like pre-injection conditions provided by the Colorado School of Mines (CSM) diesel engine simulator [6], [7]. When applied over a range of gas temperatures, pressures, and fuel types, ballistic images of the near-orifice region provide a valuable benchmark data set for development of advanced atomization and spray models. For example, picosecond ballistic imaging results for high-injection-pressure diesel sprays show qualitative agreement in the size and shape of spray shedding structures observed in diesel sprays [2], [4], [6], [8].

The path-averaged nature of ballistic images obscures embedded structures within the spray. A new laser sheet scattering technique is also reported here captures structures within the spray by imaging two-dimensional cross sections of the spray. Traversing the spray with the laser sheet allows us to probe within the spray for the presence of a liquid core and better understand jet breakup in the near-nozzle region.

### **1.1 Literature review**

Research efforts have focused on the implementation of the ballistic imaging technique to probe structures in the near-orifice region of high-pressure diesel sprays. The motivation to choose ballistic imaging stems from the desire to reveal intricate spray structures which otherwise are not discernible via other methods. Through the use of an ultra-fast shutter, the ballistic imaging technique captures photons that have passed through an optically dense spray with minimal scattering events. Rejection of scattered light is vital to producing an image of the true structure of the spray. Scattered photons are in effect noise added to the small number of ballistic photons that carry image information that shows the complex liquid structures within the spray. The detailed structures captured in these ballistic images will help improve spray breakup models by providing experimental evidence for comparison with simulations. Improved understanding of the break-up region of fuel sprays enables better control of droplet size distribution, evaporation, and downstream mixing in diesel sprays, with potentially profound implications for improved diesel cycle efficiency and reduced emissions.

In order to capture the true nature of the droplet field of a diesel spray, measurements must be non-intrusive. This is achieved by observing the interaction of a laser with the droplet field. Close to the injector orifice, the high number densities and attenuation levels in the spray make monitoring droplet sizes a non-trivial challenge [7]. Multiple scattering, which results from photon interaction with a dense droplet field, causes methods such as Phase/Doppler [9], [10] to be ineffective in this region of the spray. Additionally, measurements which rely on separate images of droplets [11] are similarly limited in their application due to multiple scattering. Signal attenuation of visible wavelengths in the dense spray regime near the injector tip marginalizes the effectiveness of ensemble light scattering techniques such as low-angle laser light scattering (LALLS) [12], [13]. At obscuration levels greater than 50%, diffraction based instruments' [14] requirement for empirical or theoretical corrections [15] render them of limited use in dense sprays. Polarization ratio measurements [13] can probe large optical depths, but are limited by their dynamic range capabilities; questions regarding droplet sphericity also make interpretation of polarization ratio measurements difficult.

The use of synchrotron generated x-rays has been used to image fuel sprays in the near-orifice region of non-evaporating fuels. X-ray imaging has successfully measured fuel mass fraction [16], fuel velocity fields [17], and the effect of gas-density on penetration length. Also, x-ray imaging has yielded information about fluid behavior inside the injector nozzle [18]. However, the use of x-ray radiation for imaging is not without significant challenges. X-ray imaging does not have the temporal resolution to capture the transient nature of diesel sprays, producing time-averaged images. Further, the need for tracer seeding for adequate absorption of x-ray radiation in fuel sprays, questions regarding how well the distribution of tracer material mirrors that for the fuel, and the limited potential for usage in wider engine studies due to the need for a synchrotron are among these challenges. To date, no x-ray imaging results have been reported on fuel sprays in evaporating or combusting environments. Additionally, recent modeling results of phase-contrast x-ray imaging indicate significant problems in the use of the technique for imaging dense sprays [19] [20].

Via the use of ballistic imaging techniques, investigations of the optically dense region of sprays are possible. The resulting shadowgraph- or schlieren-type images reveal structures, which are embedded inside a turbid field [20]. Conflicting predictions about the nature of the spray's core, from it having a negligible core [15] to a liquid core that extends up to 100 jet diameters [21], make the identification of embedded structures especially relevant. Previous studies at CSM have demonstrated the utility of ballistic imaging for dense sprays [22], [23]. Furthermore, work at CSM has revealed significant mixing structures on the periphery of sprays injected into an ambient atmosphere [24], [6]. Ballistic imaging of diesel sprays at engine-relevant temperatures and pressures has only recently been achieved. Our group reported the first ballistic imaging of a dodecane spray injected into air at temperatures to 600 °C and pressures to 20 atm in 2012 [6]. Falgout et. al. have recently reported fs ballistic images of dodecane injections under ECN Spray A conditions (900K, 60 atm) [25]. Here we report on ps ballistic images of dodecane injection over a range of gas temperatures and pressures as well as different fuel types.

## **2. Ballistic Imaging Characterization**

A careful characterization of the picosecond ballistic imaging technique was performed. This characterization used a scattering cell to explore the limits of imaging at high optical depth, as well as the effectiveness of the optical Kerr effect gate, spatial filtering of scattered light, and polarization filtering.



## 2.1 Experimental Methods

The experimental setup for ballistic imaging includes a short-pulse laser, an optical train with well-controlled polarization, a telescopic imaging system, a delay line, an optical Kerr effect (OKE) gate, and a scattering medium (here a scattering cell or spray). Efforts at CSM have focused on the development of picosecond ballistic imaging, where a picosecond laser is used instead of the more expensive and complex femtosecond laser system [23]. For example, the picosecond laser used in this research retails for ~\$100,000 compared to over \$350,000 for a typical femtosecond laser. The larger bandwidth of femtosecond pulses also leads to dispersion effects, which further complicate the optical train. The longer pulse length of the picosecond laser limits the maximum optical depth that can be successfully imaged, but as shown here, is capable of imaging diesel sprays.

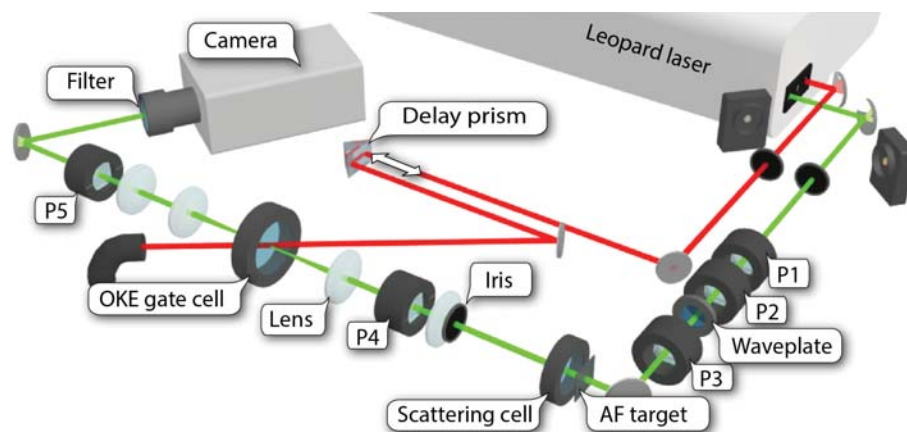


Figure 1: Experimental schematic of ballistic imaging optical train for characterization experiments. A polystyrene sphere suspension and Air Force target provide a well-characterized scattering medium and image. P1-P5 are polarizers. Beams are shown cw for clarity.

### 2.2.1 Ballistic imaging optical train

A schematic of the optical setup is shown in Figure 8 with the 532nm output from a Coherent Leopard D-10 laser operating at 10 Hz repetition rate with  $12 \pm 1$  mJ per pulse used to image the spray and the 1064 nm output ( $15 \pm 1$  mJ per pulse) used as the OKE gate beam. The OKE gate beam traveled across the table to a prism mounted on a translation stage and was then directed through a carbon disulfide ( $\text{CS}_2$ ) cell. This part of the system is known as the delay line and is used to produce an overlap, in space and time, of the gate beam and the imaging beam (Figure 2). The OKE gate was formed by a pair of crossed polarizers, P4 and P5, and the  $\text{CS}_2$  cell. P4 was oriented to pass the non-scattered image beam, while the output linear polarizer (P5) of the OKE gate was set to be crossed with P4. The key to time gating is inducing temporary birefringence in the  $\text{CS}_2$ , which is a result of a nonlinear interaction of the gate beam with the carbon disulfide [26]. In the absence of the gate beam, the crossed calcite polarizers P4 and P5, which have extinction ratios greater than  $10^{-5}$ , block all laser light from reaching the camera, thus forming a high-speed optical shutter.

Polarizers P1-P3 are used to adjust the image beam intensity and to create the correct polarization of the imaging beam. The two sets of iris-detector pairs placed near the laser in the path of each beam are used for timing and triggering of the camera. A series of four lenses are used in combination with the camera's macro lens to create a highly magnified image of the spray. For the characterization experiments, an Air Force target was placed at the image plane of the camera followed by an optical cell filled with a polystyrene sphere suspension in water. The Air Force target has well characterized groupings of lines to measure the resolution of the images, while the scattering suspension simulates the droplet scattering experienced in a spray.

An iris is placed in the optical path after the scattering cell to limit the solid angle of collection of the camera and reject a portion of the multiply scattered photons from reaching the camera.

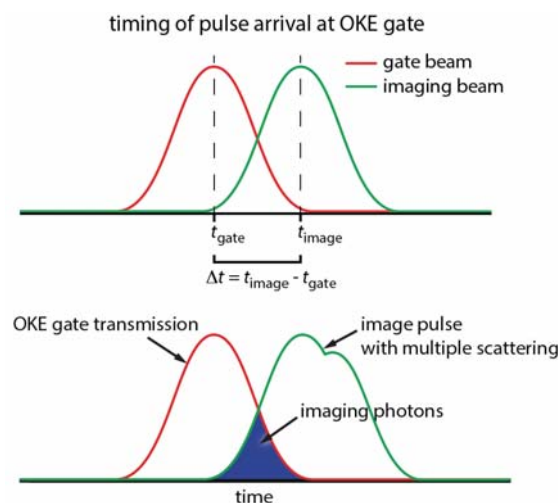


Figure 2. Schematic diagram of the time overlap of the imaging beam and gate beam at the optical Kerr effect shutter. Changing this overlap in time effectively changes the “on” time for the shutter.

### 2.2.2 Image capture

Two cameras were used for this study: a Photometrics Cascade:650 imaging array (653x492, 7.4  $\mu\text{m}$  pixels) was used for the scattering cell measurements and shadowgraphy imaging, and a CoolSNAP Myo 20MHz 2.8Mpixel digital camera (1940x1460, 4.54 micron pixels) was used for the ballistic images of sprays. Both cameras are designed for low-light applications, and were used in conjunction with various neutral density filters and a 532nm narrow band pass filter to optimize signal levels and to filter stray light.

The illumination for the images was provided by a Continuum® Leopard D-10 laser, which operates at 10Hz and is capable of 30mJ, 15 picosecond pulses at 1064nm. Compared to the femtosecond lasers used by other groups to achieve ballistic images, this setup only requires one laser to operate. The Leopard is a relatively inexpensive (~\$100,000) system capable of emitting pulses at 266, 355, 532 and 1064nm – a multi-wavelength capacity that lends more diagnostic capacity to the user.

### 2.3 Method Characterization

The picosecond ballistic imaging technique combines spatial filtering and temporal filtering to reduce the number of multiply scattered photons reaching the camera. Here we quantify the impact of each of these filtering methods on the image resolution and quantify the impact of the optical depth of the scattering medium.

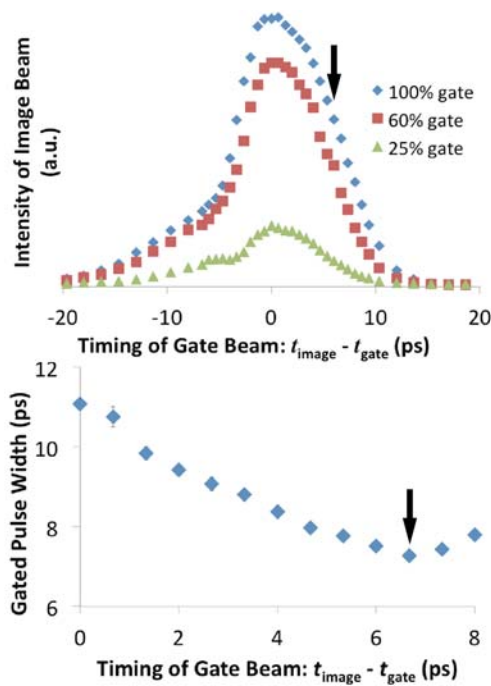


Figure 3. Performance of the Kerr cell as measured by autocorrelation. Image beam intensity decreases with increasing delay between the arrival of the gate and image beam at the Kerr cell (top). The ideal delay between gate and image beams yields the minimum gate width of 7 ps. The arrow indicates the timing used in these experiments.

### 2.3.1 Optical Kerr effect shutter

Picosecond ballistic imaging relies on precise timing of the optical Kerr effect shutter. The OKE gate beam can be delayed relative to the arrival of the imaging pulse as shown schematically in Figure 2. The imaging pulse arrives after the OKE gate is turned “on” by the OKE gate pulse. By varying the timing of the gate beam, the quality of the images can be adjusted as more or less scattered photons are transmitted onto the image plane during capture. Figure 2 depicts a stylized cartoon of the effect that gate and image beam overlap (shown in blue) has in picosecond ballistic imaging. If the gate beam arrives too early, the overlap area is reduced and too few photons reach the camera resulting in an image with high noise and poor resolution. Alternatively, if the gate beam arrives too late, the overlap area is large but includes a larger percentage of scattered photons, blurring the image.

The best results achieved to date are with the Kerr cell transmission beginning to switch “off” just as the image pulse arrives at the Kerr cell (see Figure 2), resulting in transmitted imaging pulses of about 7ps (Figure 3). Pulse width was measured by autocorrelation, which revealed slightly asymmetric Gaussian transmitted pulses consistent with a parent Gaussian beam that has the asymmetry of the 2 ps relaxation time from CS<sub>2</sub> superimposed on the pulse transmitted by the gate. The full-width-half-maximum (FWHM) values of the transmitted pulse are shown in Figure 3 and were measured with varying delay between the image and gate pulses. The gate beam intensity was also varied to measure the impact of gate beam intensity on the intensity of the transmitted image beam. Although nonlinear, a more powerful gate beam resulted in more light transmission through the OKE gate. Subtle changes in the timing of the imaging and gating beams utilized to capture these images can result in ballistic vs. non-ballistic results.



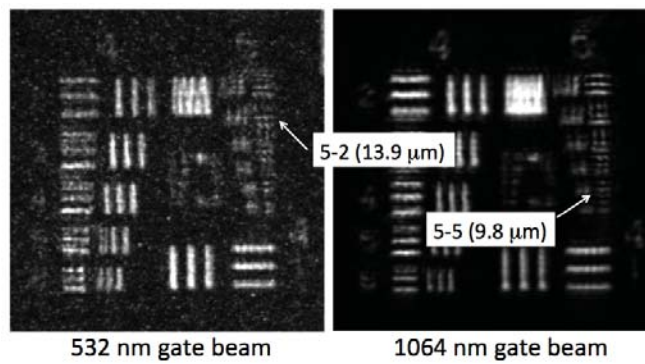


Figure 4. Air Force target images using a 532nm switching beam (left) and a 1064 nm switching beam (right). Images collected without any scattering medium present.

As others have shown [27], [28], using different wavelengths for the gate and imaging beams prevents scattering of the gate beam from contaminating the transmitted image. To demonstrate this, an Air Force target was imaged through the OKE gate with a 532nm and 1064 nm gate beam, respectively (Figure 4). Scattering from the 1064nm gate beam was rejected by the 532nm filter on the camera and resulted in reduced image noise and increased resolution. The multi-wavelength capability of the picosecond laser allows for one laser to be used for both switching and imaging beams—a distinct advantage over other two-laser BI systems.

Over time the high intensity of the gate beam breaks down the CS<sub>2</sub> leading to buildup of precipitates in the CS<sub>2</sub> cell. Even with periodic replacement of the CS<sub>2</sub>, large shot-to-shot variations in transmitted image beam intensity were observed during autocorrelation. These fluctuations were hypothesized to be caused by induced thermal gradients in the CS<sub>2</sub> due to local heating. To reduce this fluctuation and extend the life of the CS<sub>2</sub>, a flowing Kerr cell was designed. Continuously recirculating the CS<sub>2</sub> removed the shot-to-shot fluctuations.

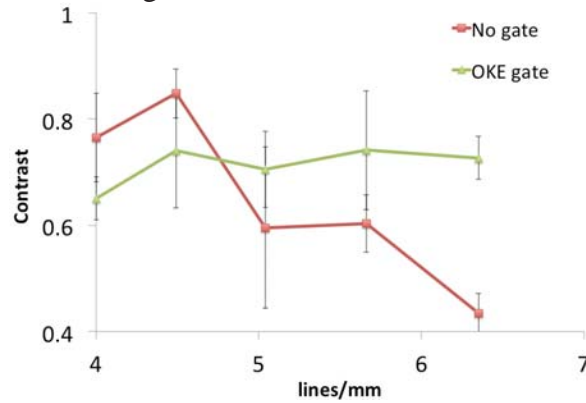


Figure 5. CTF calculated from an Air Force target imaged through a 20mm cell filled with 5  $\mu$ m polystyrene spheres suspended in water (OD = 6.71). Spatial filtering was used with a solid angle of collection of  $\Omega = 0.002$  sr. At 20mm, the OKE gate has a measureable effect on CTF. Data points represent the average of 3 line pairs with error bars equal to the standard deviation.

### 2.3.2 Temporal filtering

To test the effectiveness of the OKE gate, the imaging beam was passed through an Air Force target followed by a scattering cell filled with suspended polystyrene spheres. Three different path length cells were used: 2mm, 10mm, and 20mm. Images were collected using each cell with the OD varied between 0 and 9. The OD was measured by removing the Air Force target and placing an optical power meter at P4 in Figure 8. The power meter measured the imaging beam power with and without the scattering cell in place. The OD was calculated from Beer's law as the negative natural log of the ratio of the two measured powers. It is important to note here that the Air Force target was placed before the scattering cell instead of in the middle of the

cell as others have done [29], [30]. Although the total OD is unchanged, placing the target in the middle of the scattering cell reduces by a factor of two the level of image scattering. As a result, previous experiments with femtosecond ballistic imaging through scattering cells have achieved optical depths as high as 13, whereas our results show a maximum OD of 9. Thus care should be taken in directly comparing results between ballistic imaging scattering cell experiments.

Using path lengths of 2mm and 10mm, and for all values of OD, we found no measurable improvement in image quality when using the OKE gate. At short path lengths (e.g. 2 mm) with  $OD < 10$ , the delay between ballistic and multiply scattered photons is on the order of 1-3ps [20]. Thus, the 7 picosecond gate employed here has limited impact for short path lengths. Another potential reason for poor OKE gate performance may be imperfections in the polarizers used, as image degradation was observed with the OKE gate in place. There was however a measurable improvement for line pairs greater than 5 lp/mm at a path length of 20mm and high OD, as shown in Figure 5. The contrast transfer function, CTF, for a 20mm path length cell with an OD of 6.7 was calculated using the Air Force target by monitoring the intensity through a three-line pattern. CTF was calculated using  $CTF = (I_{max} - I_{min}) / (I_{max} + I_{min})$ , where  $I_{max}$  is the peak image intensity on a single line, and  $I_{min}$  is the minimum image intensity between adjacent lines. This was repeated for all lines in a three-line set and the average of the three was plotted as a single data point in Figure 5. The CTF revealed that the OKE gate improved image resolution for a 20 mm path length with high OD.

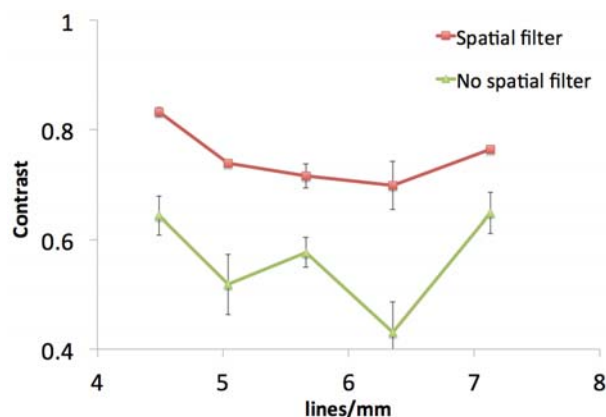


Figure 6. CTF of Air Force target images captured using 10mm scattering cell (OD = 8.35) with and without spatial filtering. Images were taken without OKE gate.

### 2.3.3 Spatial filtering

As others have shown [31], [32], limiting the solid angle of collection in ballistic imaging improves image resolution by preventing a portion of the single and multiply scattered light from being collected by the camera. As light travels through the scattering medium, photons passing through scattering objects (droplets, ligaments, etc), will undergo an elastic scattering event that changes the direction of the photon. This change in direction depends upon the scattering medium, the scattering particle size, and the wavelength of light. For a single scattering event typical of micron-sized droplets, the majority of visible light is scattering in the forward direction at small angles relative to the initial direction of the photon. In dense scattering media, photons will experience more than one scattering event, or multiple scattering. As multiple scattering increases, the angular direction of the scattered light approaches a uniform distribution in  $4\pi$  steradians (i.e. the light is scattered uniformly in all directions). Thus, greater levels of multiple scattering increase rejection of scattered photons by spatial filtering.

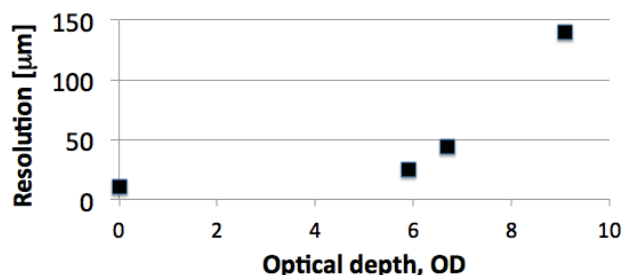


Figure 7. Highest resolution image achieved at increasing optical depth. Resolution decreases with increasing OD. Resolution was determined from the highest number of lines/mm discernable on the Air Force target.

The impact of spatial filtering on image resolution is shown in Figure 6. Spatial filtering was accomplished by placing an iris 200mm after the Air Force target with a diameter of 1cm, providing a solid angle of collection of 0.002 sr. A CTF of the Air Force target imaged at OD=8.35 shows a significant improvement when spatial filtering is used. In fact, we found that spatial filtering had a more significant impact on image resolution than the OKE gate for all path lengths and optical depths studied.

### 2.3.4 Overall imaging performance

Combining the effects of spatial and temporal filtering results in an imaging system that is able to collect images at very high optical depths. The maximum resolution using the 2mm cell at each OD is plotted in Figure 7. At low OD, the imaging system is able to resolve features as small as 10  $\mu\text{m}$ . In sprays, low OD fine features along the periphery can be successfully imaged using this technique. As the OD increases, the resolution degrades, preventing fine features embedded in high OD regions of the spray from being successfully imaged. Thus, fine features in the core of the spray are not accessible with this imaging method and should be studied either with shorter pulse ballistic imaging or with x-ray imaging.

## 2.4 Conclusions

The characterization and demonstration of a 15 picosecond 532nm Nd:YAG laser-based ballistic imaging system is reported. A CS<sub>2</sub> OKE gate activated by a 1064nm switching beam was measured to have a 7ps gate width using autocorrelation. A two-color OKE gate system was also shown to have superior image quality due to removal of gate beam scattering. The impact of spatial filtering and temporal filtering on image quality were measured using an Air Force target imaged through a variable path length scattering cell of 5 $\mu\text{m}$  polystyrene spheres suspended in water. The 7ps OKE gate was observed to have little effect on image quality for scattering cell path lengths of 2mm and 10mm. A measurable improvement in image resolution was observed at a pathlength of 20mm at optical depths > 6. Successful imaging through scattering cells with optical depths to OD 9 are reported and show decreasing image resolution with increasing OD, with a maximum resolution of 10  $\mu\text{m}$ .

## 3.1 Diesel Spray Imaging

This effort is focused on a combination of developing the optical tools to probe the high-density region of a diesel spray and the use of these tools to improve our understanding of near-orifice spray behavior. Images taken near the injector orifice provide a valuable benchmark data set for development of advanced atomization and spray models. This work is based on a unique capability developed at the Colorado School of Mines (CSM) relevant to improvements in diesel engine technology. This experimental capability includes the ability to produce very controlled, diesel-like pre-injection conditions along with non-intrusive diagnostics specifically developed

to monitor the near field of diesel sprays. The purpose of the facility and diagnostics being to investigate the controlling breakup modes of diesel sprays for operating ranges relevant to diesel engines.

## 3.2 Experimental Methods

Application of picosecond ballistic imaging to diesel sprays in pressure and temperature regimes relevant to actual diesel engine operating conditions has been the focus of efforts at CSM. The experimental setup required includes the ballistic imaging optical train, image capture and post processing, a fuel injection system, the heated pressure vessel, and process control and data acquisition hardware. Each of these components is described below.

### 3.2.1 Ballistic imaging optical train

The 532nm output of a Coherent D-10 laser with pulse energy of  $12 \pm 1$  mJ and a 10 Hz repetition rate is directed as shown in Figure 8. Upon exiting the laser, the pulse is split into two legs by a 90/10 beam splitter. The higher energy pulse is used as the OKE (optical Kerr effect) switching beam, whereas the lower energy pulse is used for imaging purposes. The OKE beam traverses the table to a prism, which is attached to a translation stage and subsequently directed through a CS<sub>2</sub> Kerr cell. Located at an intermediate plane in close proximity to the Fourier plane of the imaging beam, the OKE cell is activated by the switching beam, which enters at an angle of 11° from normal. A translation stage creates the delay line, which is used to control the overlap, in space and time, of the gate beam relative to the imaging beam in the Kerr cell (see Figure 2). Two crossed 20mm cube polarizers, P4 and P5 and the CS<sub>2</sub> cell make up the complete OKE gate. P4 is oriented to pass the image beam in its non-scattered state, whereas the output linear polarizer (P5) is set to be crossed with P4. Time gating produced via this setup is dependent on the rotation of the polarization state of the image beam, which is the result of the interaction of the carbon disulfide and the gate beam.

The optical train for the image beam consists of two polarizers, P1 and P2, which are oriented to match the vertical polarization of the parent laser pulse and are used to assure clean polarization. After the polarizers is a ½ wave plate, which is used to control energy levels in the imaging beam. Following the wave plate is a polarizer, P3, which is set to be 45° with regards to P1 and P2, and in the same orientation as P4 of the OKE gate. Additionally, the image train contains four lenses, which are used to achieve two separate purposes. First is to focus the image beam down so that it is completely contained within the radius of the switching beam while overlapping in the CS<sub>2</sub>, and secondly to form a telescopic effect at the imaging plane. Optimization of the image train was conducted using Zemax® software.

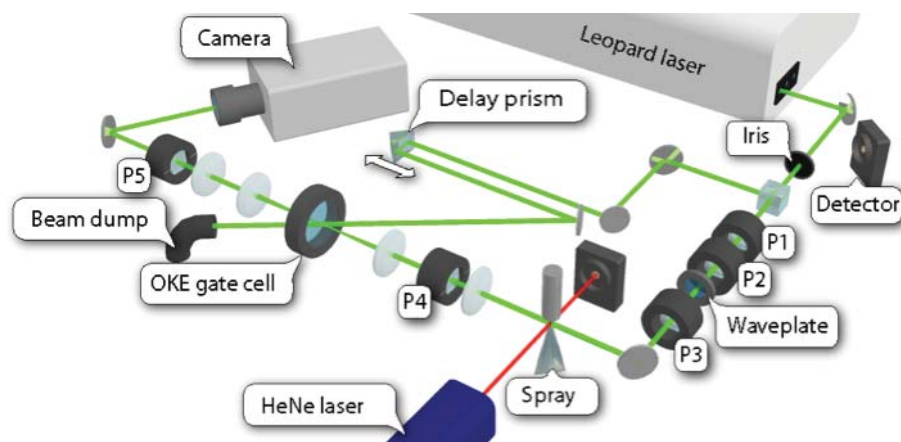


**Figure 8: Experimental schematic of ballistic imaging optical train.** The HeNe laser and separate detectors are to measure the arrival of the imaging pulse and the spray injection timing. P1-P5 are polarizers. Beams are shown as cw for clarity.

### 3.2.2 Image processing

In order to create an image of optical depth, a series of image processing steps were undertaken for each image (Figure 9). Prior to capturing spray images, a series of images were taken with the lens cap on the camera (background images). Additionally, images were captured of the laser with no spray, which constituted the baseline images. These series of images were then averaged and were labeled background ( $B$ ) and baseline ( $I_o$ ) respectively. Finally, the image of the spray was captured (labeled  $I$  in Figure 9). A background subtracted optical depth image was created using Beer's law. As can be seen from Figure 9, capturing a baseline is essential to achieving low noise images of sprays. The combination of laser speckle, refraction, and beam profile intensity variation in the image would otherwise interfere with spray features. All images were processed as outlined in Figure 9.

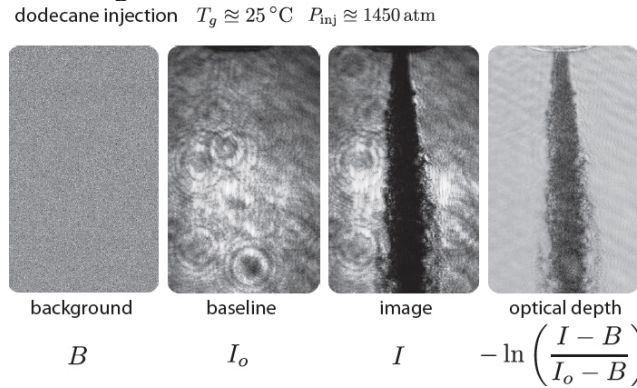


**Figure 9: A visual guide to the image processing steps used in capturing ballistic images of sprays.** These images were collected with the Cascade camera.

### 3.2.3 Image capture

In order to capture images inside the pressure vessel, a timing scheme was designed to sync the laser pulse with the camera system and the injector firing (Figure 10). The timing of the trigger pulse was set by a photodiode that measured scattered light from an optic in the optical train. This photodiode signal was sent to a pulse generator, which in turn generated the triggering pulse for the image capture timing. The 10 Hz triggering pulse train was passed to a custom programmed PIC controller box, which also received an operator command to fire the injector. Upon receiving a request for an injection event, the injector controller fires the injector at a timing that coincides with the laser pulse passing through the spray. By adjusting the delay between the laser pulse sensed by the photodiode and the output pulse from the signal generator, the user can control the arrival time of the laser pulse to the spray with respect to the beginning of the injection event. In addition to communicating with the injector controller, the PIC also sent a TTL pulse to the camera, which effectively produced an image capture signal that enveloped the time period when the laser pulse is present. This pulse is delayed via a second pulse generator. By utilizing both pulse generators the user can adjust the timing of the image of the spray, relative to the beginning of the spray.



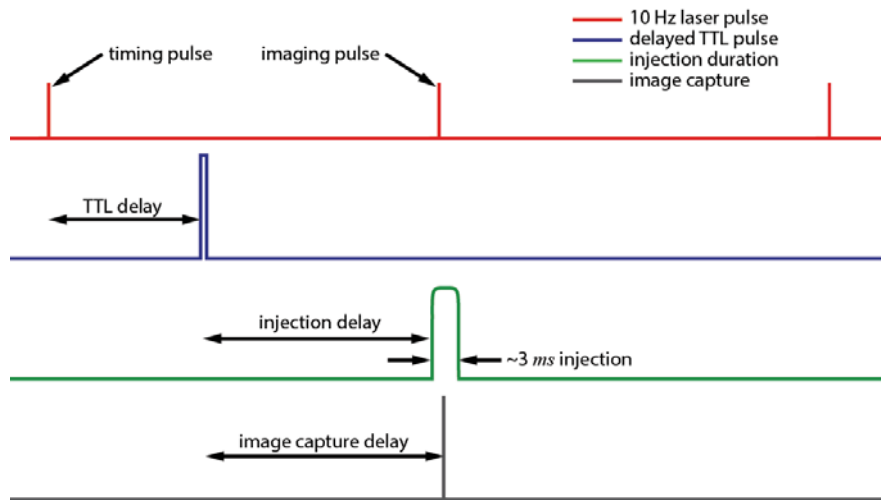


Figure 10: A schematic of the electronic timing used during imaging.

The camera was a Photometrics Cascade:650 imaging array (653x492 pixels, each  $7.4 \mu\text{m}$  square). This camera is designed for low-light applications, and was used in conjunction with an ND 2.0 filter and a 532 nm band pass filter to optimize signal levels and to filter stray light. Spray duration was tracked using a HeNe laser beam aligned to cross directly below the tip of the injector. The HeNe beam was directed to a detector and monitored on an oscilloscope. Spray duration, as determined by attenuation of the HeNe beam, was typically 3.0 to 3.5 ms. The imaging beam was monitored via a photo detector on the same oscilloscope. The arrival time of the imaging beam relative to the initiation of the spray was determined from the oscilloscope traces.

A Continuum® Leopard D-10 laser, operating at 10 Hz, was utilized to provide illumination for the images. This relatively inexpensive laser is capable of generating 15 picosecond pulses at 1064nm with energy levels up to 30mJ. In contrast to femtosecond lasers employed by other groups, the Leopard is capable of ballistic imaging as a standalone unit. The D-10 also provides the user with the capability to generate pulses at 266, 355, and 532nm, which enhances diagnostic capability.

### 3.2.4 Diesel injection system

A Sturman Industries common-rail type diesel injector was used for all experiments. This injection system is capable of multiple pulse injections with pressures in excess of 200 MPa and was custom electrical discharge machined to include a single, on-center, injection hole  $160 \mu\text{m}$  in diameter. To prevent fuel degradation and subsequent clogging of the injector, the injector body was encapsulated in an insulated housing. Modeling of the thermal conditions revealed that the injector tip assembly maintains a maximum temperature of about  $150^\circ\text{C}$ . Cooling of the fuel is enhanced by recirculation of the fuel through the injector housing and into a cooling bath utilizing a coil-type heat exchanger. Examination of the disassembled injector shows no signs of fuel coking (normally observed at  $150\text{--}180^\circ\text{C}$ ), even after operation at chamber temperatures of  $600^\circ\text{C}$ .

Experiments utilize a custom-manufactured combustion vessel capable of maintaining pre-injection conditions of 50 atm and 1000 K. As shown in Figure 11, the diesel engine simulator was split into an inner heated core surrounded by an exterior pressure vessel. The exterior pressure vessel has four orthogonal, purged optical ports for line-of-sight optical measurements and detection at  $90^\circ$ . The inner heated core is the central air-bearing region and is 44.5 mm in diameter. The distance from the injector tip to the opposing wall is adjustable. Further details of

the experimental system and gas extraction can be found in the literature [19] and are summarized in Table 1.

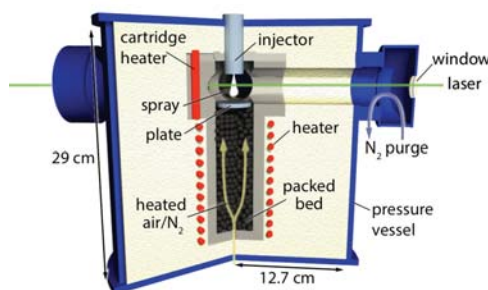


**Figure 11: The Diesel Engine Simulator. Air or nitrogen is preheated by packed bed of steel ball bearings. Fuel is injected into the heated chamber toward a steel plate, which simulates the top surface of a piston.**

Due to the range of engine designs and operating conditions there is no “standard” diesel combustion event. Experiments conducted in the simulator described in this paper were designed to emulate a number of the important characteristics of diesel combustion. As shown in Table 1, the simulator effectively replicates most of the important characteristics of diesel combustion. The most striking difference between the simulator and engines, in terms of operating parameters, is pressure. The simulator was operated at 20 atm versus the 30 atm and greater typical of diesel engines; additionally, the simulator is isobaric.

**Table 1. Comparison of typical diesel engine characteristics with the Diesel Engine Simulator.**

Characteristic	Engine	Simulator (for most recent work)
Injection Pressure	30-150 MPa[33], 20-80 MPa[33], 100-150 MPa[34], 20-170 MPa[35]	55-150 MPa
Nozzle orifice diameter	0.15-0.35 mm [33], 0.184 mm[34], 0.194 mm	0.160 mm
Nozzle orifice L/D	2-8[35], 4	4
Number of nozzle orifices	3-8 holes	1 hole
Types of nozzles used	Pintle and Hole-type nozzles	Hole-type nozzle
Mass injection	2-24 mm <sup>3</sup> per hole[36]	4 mm <sup>3</sup> min.; 37 mm <sup>3</sup> max.
Chamber temperature	1000-1200 K, 700-1300 K [37]	873 K
Chamber pressure	40-120 atm [33], 50-100[35]	20 atm (plans for 35 atm)
Hard wall interaction length	50-60 mm[37]	100 mm
Liquid length	18 mm	30 mm
Change in chamber pressure	6 MPa[37]	25 kPa
Compression ratio	16-22[35]	None
Overall stoichiometry	Fuel lean[35]	Fuel lean

### 3.2.5 Orthogonal imaging

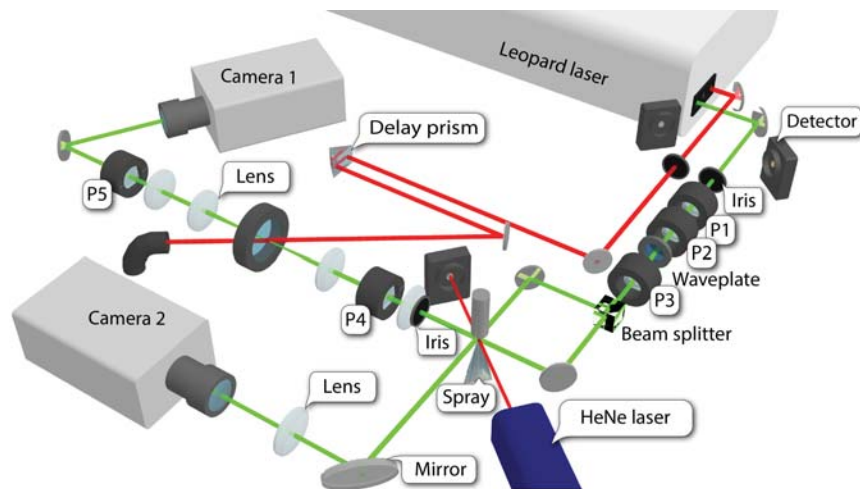


**Figure 12.** Optical layout for simultaneous orthogonal imaging of a fuel spray using ballistic (camera 1) and shadowgraphy (camera 2) techniques.

The complexity of the ballistic imaging optical train may raise the question of whether this type of imaging is required to study the near-orifice region of diesel sprays. To quantify improvements in image resolution and clarity, sprays were imaged simultaneously using the ballistic imaging technique, with spatial filtering (solid angle of collection of  $\Omega = 0.002$  sr), and with traditional shadowgraphy. To accomplish this, the imaging beam was passed through a 50/50 beam splitter and into orthogonal optical paths (Figure 12). The Myo camera was used for the ballistic imaging line (Camera 1), while the Cascade camera was used for the shadowgraphy experiments (Camera 2). Two identical cameras were not available at the time of these experiments, so the resolution of the two images has been matched via image post processing in Matlab (Figure 13).

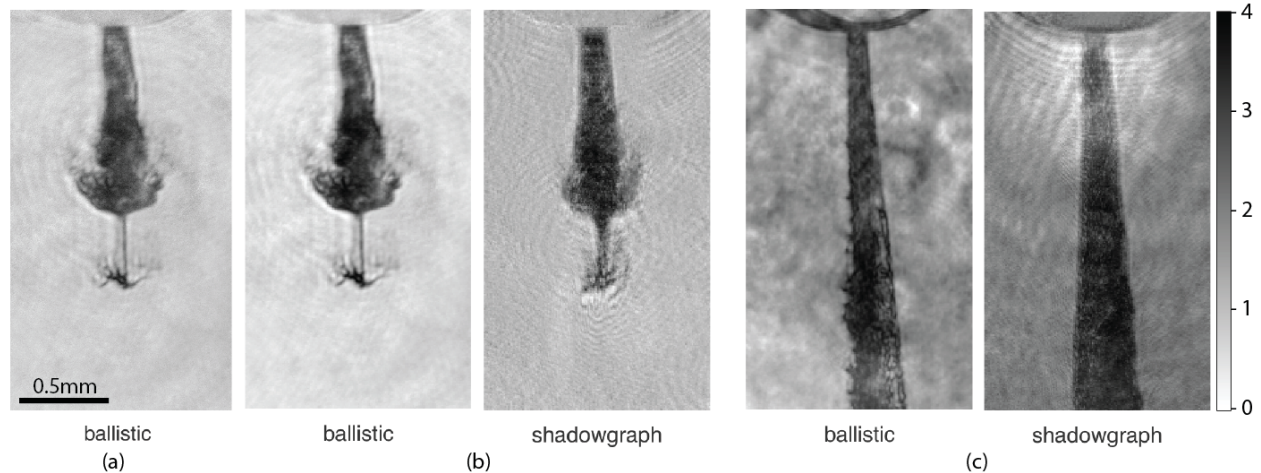


**Figure 14:** Orthogonal and simultaneous ballistic images and traditional shadowgraphs of a methyl butyrate spray (a-b) and a methyl oleate spray (c) injected at 1450 atm into ambient air. Image resolution for the ballistic image in (a) is 500 x 900 and 170 x 300 for the images in (b) and (c). The ballistic images in (b) and (c) were post processed to reduce their resolution to match the shadowgraph images. The scale of optical depth, OD, is shown in the color bar on the right.

Sample results from the simultaneous orthogonal imaging are shown in Figure 15. The 1450 atm injection pressure sprays were injected into ambient air. As can be seen, shadowgraphy captures the overall shape of the spray, but does not capture finer structures such as liquid ligaments and voids. Further, shadowgraphic images of the spray sometimes appear wider than the ballistic image due to scattering on the periphery of the spray where droplet loadings are significant. In contrast, the ballistic images show detailed structure on the order of tens of microns and reveal



voids within the spray. This higher resolution is critical to understanding spray breakup physics and obtaining quantitative data on liquid ligament formation, frequency, size, and velocity.

### 3.3 Diesel Spray Imaging Results & Discussion

Two types of fuels have been investigated: dodecane and methyl oleate. Dodecane is a common diesel fuel surrogate and methyl oleate is a common bio-diesel surrogate. Several different test regimes were examined and will be presented individually and then compared in terms of observed trends. These include:

- Dodecane injected into ambient air at varying injection pressure (Table 2. Rows 1-2)
- Dodecane injected into room-temperature air at elevated air pressures (Table 2. Row 3)
- Dodecane injected into air at elevated temperature and pressure (Table 2. Rows 4-6)
- Methyl oleate injected into ambient air (Table 2. Row 7)

**Table 2. Operating conditions tested, corresponding fuel properties [38]–[40], and non-dimensional groups.**

	temp (liq) (°C)	temp (charge) (°C)	pressure (charge) (atm)	pressure (injection) (atm)	velocity (m/s)	liquid density (kg/m <sup>3</sup> )	surface tension (N/m)	liquid viscosity (Pa-s)	Re (-)	We (-)	Oh (-)
dodecane	1. 25	25	1	970	514	744.4	2.49E-02	1.32E-03	4.65E+04	1.26E+06	2.41E-02
	2. 25	25	1	1500	639	744.4	2.49E-02	1.32E-03	5.79E+04	1.95E+06	2.41E-02
	3. 25	25	20	1450	623	745.8	2.49E-02	1.35E-03	5.52E+04	1.86E+06	2.47E-02
	4. 150	600	3	1450	672	650.0	1.39E-02	3.21E-04	2.18E+05	3.38E+06	8.45E-03
	5. 150	600	12	1450	669	651.5	1.39E-02	3.26E-04	2.14E+05	3.36E+06	8.57E-03
	6. 150	600	20	1450	666	652.7	1.39E-02	3.30E-04	2.11E+05	3.35E+06	8.67E-03
methyl oleate	7. 25	25	1	1450	581	868.8	2.90E-02	5.32E-03	1.52E+04	1.62E+06	8.38E-02

For reference in comparing imaging results from different fuels and conditions, Table 2 has been compiled, which contains the majority of the experimental conditions with accompanying fuel properties and non-dimensional groups. Reynolds, Weber, and Ohnesorge numbers were evaluated using the following equations from fuel properties and injection parameters [41].

$$\text{Re} = \frac{\rho_l LV}{\mu_l}, \quad \text{We} = \frac{\rho_l LV^2}{\sigma}, \quad \text{Oh} = \frac{\text{We}^{1/4}}{\text{Re}} = \frac{\mu_l}{(\rho_l \sigma L)^{1/4}}$$

where  $\rho_l$ ,  $\mu_l$ ,  $\sigma$ , and  $V$ , are the density, viscosity, surface tension, and velocity of the liquid fuel, and the characteristic length,  $L$ , was taken as the injector orifice diameter: 0.16 mm. The velocity was calculated from Bernoulli's equation. The Reynolds number relates the ratio of inertial to viscous forces and the Weber number relates the ratio of momentum to surface tension forces and has been correlated with jet breakup regimes. The Ohnesorge number is given by the ratio of the fourth root of the Weber number and the Reynolds number and is an indicator of jet stability.

#### 3.3.1 Direct comparison of ps ballistic imaging and shadowgraphy

Two cameras were used to *simultaneously* image a single injection: the Photometrics Cascade:650 was used for the shadowgraphy imaging, and a CoolSNAP Myo 20MHz 2.8Mpixel digital camera (1940x1460, 4.54 micron pixels) was used for the ballistic images of sprays. Shadowgraphic images were acquired by splitting the 532nm imaging beam with a 50/50 beam splitter and passing one leg through the spray without any temporal or spatial filtering. The other leg consisted of the ballistic imaging train described. Complete details of this experiment have been presented in a separate publication [42].

Images of the same spray event captured simultaneously via the ballistic imaging technique and with traditional shadowgraphy show increased ability to identify small scale liquid structures on the periphery of the spray using ballistic imaging (Figure 15). There is also significant broadening of the spray with traditional shadowgraphy, which is likely due to the lack of scattering rejection in the shadowgraph. The long liquid ligaments, voids, and mass shedding evident in the ballistic image are also seen in the shadowgraph, but with much less detail.

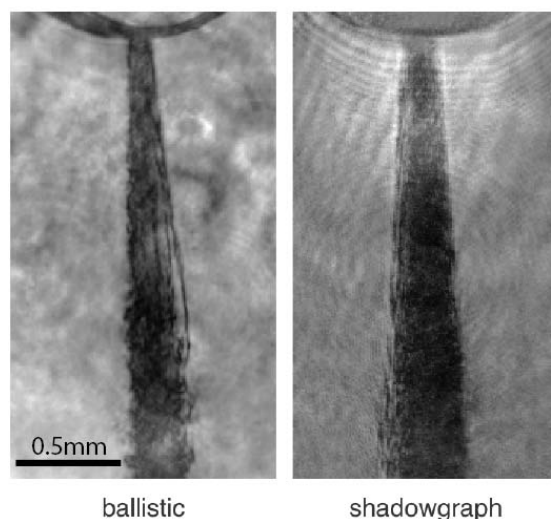


**Figure 15:** Simultaneous orthogonal imaging of a methyl oleate spray injected at 1450 atm into ambient air. Image resolution for both images is 170 x 300.

### 3.3.2 Evolution of a spray

The ballistic imaging methods discussed above, combined with controlled injection timing, allows spray behavior to be studied over the life of the spray from start of injection to end of injection as well as ignition. For example, Figure 16 shows the evolution of a methyl butyrate spray from early injection to end of injection (images are from separate injections). Early after start of injection (images 1-3), the spray plume is clearly visible, in agreement with direct numerical simulation models [8]. Also seen is the typical widening of the spray seen at early injection times (image 4) followed by spray narrowing at intermediate times (images 5-6). Finally, near end of injection, the spray begins to become unstable (image 6), and finally shuts off leaving a low velocity stream of fluid without significant atomization (image 7).

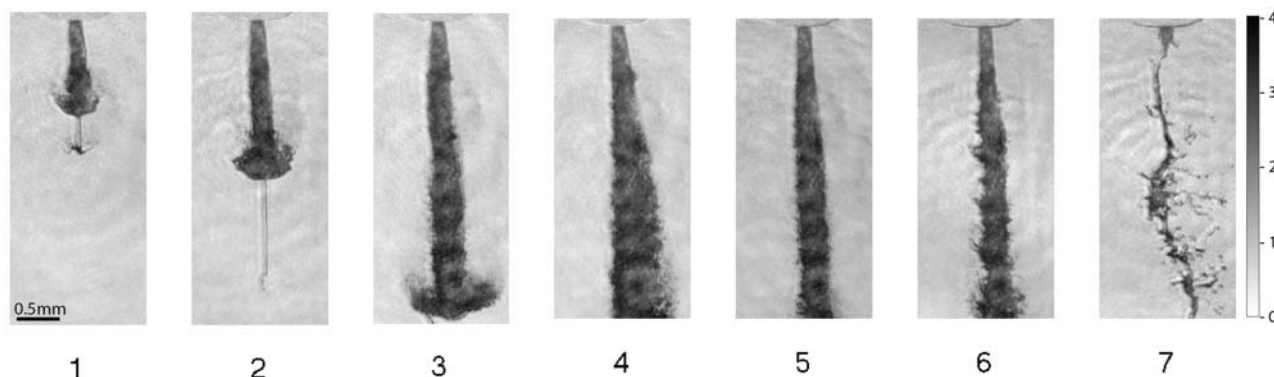


**Figure 16.** Ballistic images of methyl butyrate sprays injected at 1450 atm into ambient air and captured at increasing times after start of injection. The total duration of a typical injection is 3 ms. The scale of optical depth, OD, is shown in the color bar on the right.

### 3.3.3 Effect of fuel type on spray behavior

Ballistic imaging studies of the effect of fuel type on the near-field region of the spray show non-trivial differences in spray breakup. Figure 17 compares ballistic images of methyl oleate ( $C_{19}H_{36}O_2$ , biodiesel surrogate) and methyl butyrate ( $C_5H_{10}O_2$ , no longer considered a suitable biodiesel surrogate due to non negative temperature coefficient (NTC) behavior) sprays in an ambient air background. The methyl butyrate, which has a lower molecular weight and lower boiling point, shows significantly less spray shedding than the methyl oleate spray. The methyl oleate image also reveals very long ligaments running parallel with the spray.

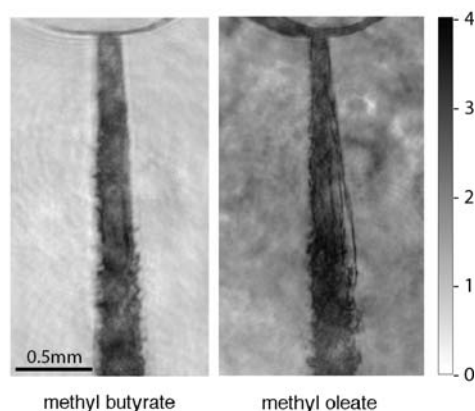
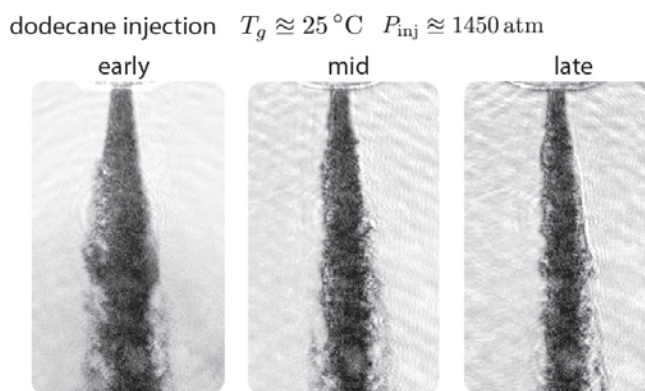


Figure 17. Comparison of ballistic images of methyl oleate and methyl butyrate sprays at 1450 atm injection pressure in ambient air. The scale of optical depth, OD, is shown in the color bar on the right.

Ballistic imaging of the near-orifice region of biodiesel sprays is reported. Orthogonal, simultaneous images of a spray using ballistic imaging and shadowgraphy, respectively, demonstrate that ballistic imaging is superior in resolving fine features in the spray. Two biofuel surrogates are compared and show that at the conditions tested, fuel type impacts spray shedding in the near-orifice region.

### 3.3.4 Transient fluctuations in room temperature dodecane sprays

The bulk of the initial imaging undertaken in this study was of dodecane at standard temperature and pressure. This phase of testing was focused on validating the system's performance and provided proof of concept testing for pulse-sliced ballistic imaging. These initial images revealed trends in the spray, which were present across the entire test matrix of fuels, temperatures and pressures. The most persistent trend observed in this phase of testing was the oscillation of the width of the spray in time (relative to start of injection) (Figure 18). Similar oscillations have been seen in all cases studied.



### 3.3.5 Injection pressure and double pulsed injection

In a separate experiment, the injection pressure of dodecane was varied from 970 to 1500 atm to examine the effect of injection pressure on the spray structure. This study revealed that at all three injection pressures, significant shedding was present on the spray's periphery (Figure 19). Other than a very slight narrowing of the spray cone angle with increasing injection pressure, there was little change in structure with increasing injection pressure.

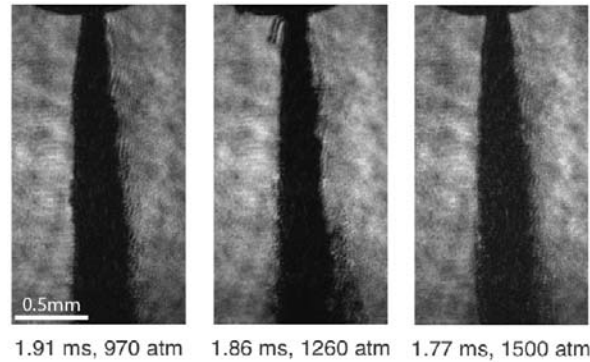


Figure 19: Ballistic images of dodecane at various injection pressures revealed significant shedding in all cases.

In yet another experiment, the injector was double-pulsed at 1450 atm injection pressure into atmospheric conditions. This test was intended to examine the effects of multiple injections in rapid succession, a strategy used in modern diesel engines to reduce sooting [43]. The images show no significant differences in spray structure, but this may be due to the 3 ms time lapse between injection pulses (Figure 20).

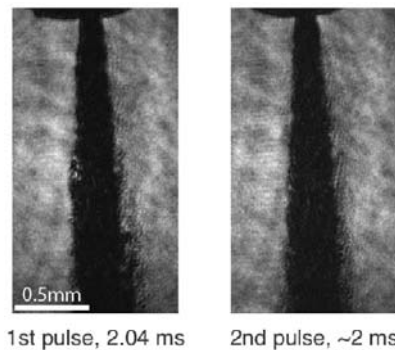
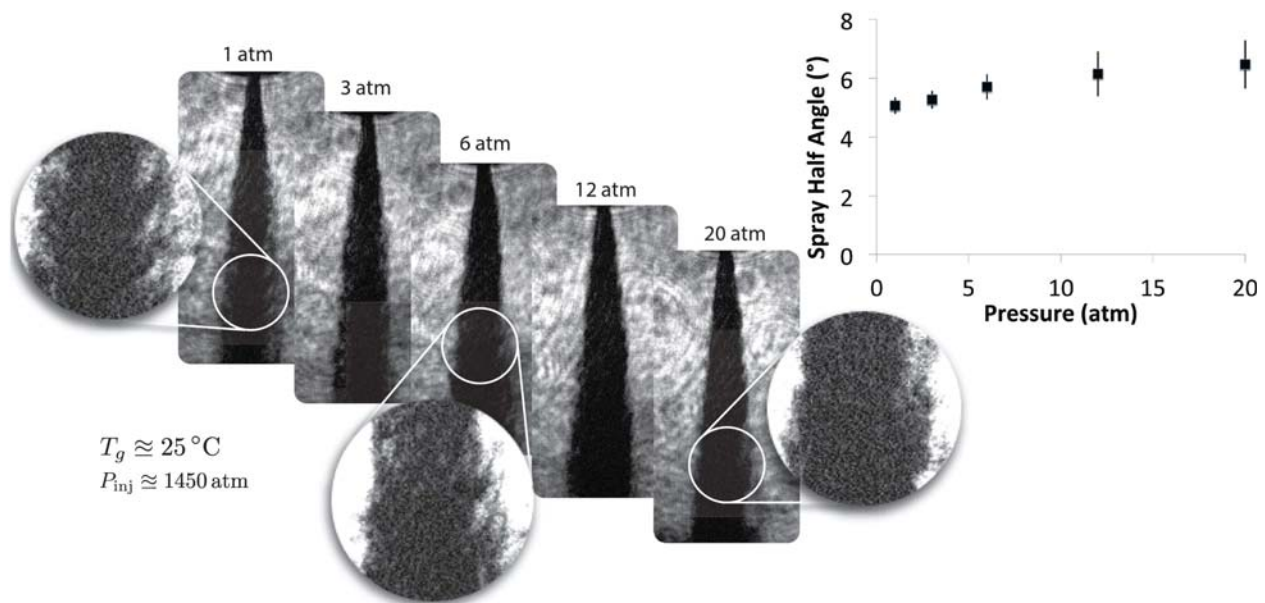


Figure 20: Images of a double-pulsed sequence of injections shows similar structure in each spray.

### 3.3.6 Effect of charge pressure on dodecane sprays

The next series of images were captured of dodecane injected into air at room temperature and increasing pressure (Figure 21). Periphery shedding of the liquid core is seen at all pressures, with slightly more shedding at low pressure, but much less pronounced than what is seen at higher air temperatures (Figure 22). These images revealed that the near-nozzle spray angle increased with increasing air pressure at ambient temperature. There was also an increase in the fluctuation of the spray angle with increased air pressure, as seen from the error bars in the inset graph.





**Figure 21:** (left) Images of dodecane at room temperature and increasing pressures. Magnification with additional contrasting highlights shedding phenomena. (right) Spray cone angle increased with increasing charge pressure. Data points are averages over ~30 images each. Error bars represent one standard deviation.

### 3.3.7 Effect of charge temperature and pressure on dodecane sprays

The most relevant testing regime to diesel engine studies was the imaging of dodecane injections at high air temperature and pressure. At these air temperatures, the liquid fuel is preheated in the injector to  $\sim 150^\circ\text{C}$  due to conduction from the heated chamber. Dodecane was injected into air at  $600^\circ\text{C}$  and pressures from 3-20 atmospheres. At the higher-pressure levels, conditions are representative of the environment found in actual diesel engines (Table 1). The higher chamber pressure and temperature caused large density gradients in the pressure vessel making it impossible to acquire quality baseline images,  $I_o$ , due to significant shot to shot variation (Figure 9). The images shown here have been converted to optical depth by taking the negative natural logarithm of each image (pixel by pixel).

The captured images revealed many trends that varied with pressure and revealed breakup structures that to our knowledge have not previously been observed in the near-orifice region, but have been predicted by others [4], [5]. Initial images revealed large differences in the observed structures compared to those observed at the same pressures but lower temperature (Figure 21). Additionally, the observed spray cone angles increased with pressure (Figure 22), similar to the low temperature sprays (Figure 21). Further examination revealed that the observed shedding structures developed nearer to the injector with increasing pressure (Figure 23). It appears that the optical density of the spray seems lower during the period of time when the shedding structures occur, which may be indicative of evaporation and mixing within the spray cone. Although a statistical analysis of the spray shedding structures has been unsuccessful due to the high background noise in the images at high pressure, spatial frequencies are observed to be approximately  $10\text{mm}^{-1}$ , with ligament lengths between  $50\text{-}200\mu\text{m}$ .

Some of the observed trends can be correlated to the data in Table 2 and some cannot. First, fuel properties are largely insensitive to the charge pressure (vessel pressure). On the contrary, fluid temperature has a more dramatic effect on density, surface tension, and viscosity. The Weber number nearly doubles as the fuel liquid temperature rises from ambient to  $150^\circ\text{C}$ , while the Ohnesorge number is reduced by a factor of three for the same temperature change. The most significant change in fuel properties is the reduced viscosity at high temperature. This reduction

in viscosity could in part explain the observed shedding structures seen in high temperature and pressure dodecane sprays.

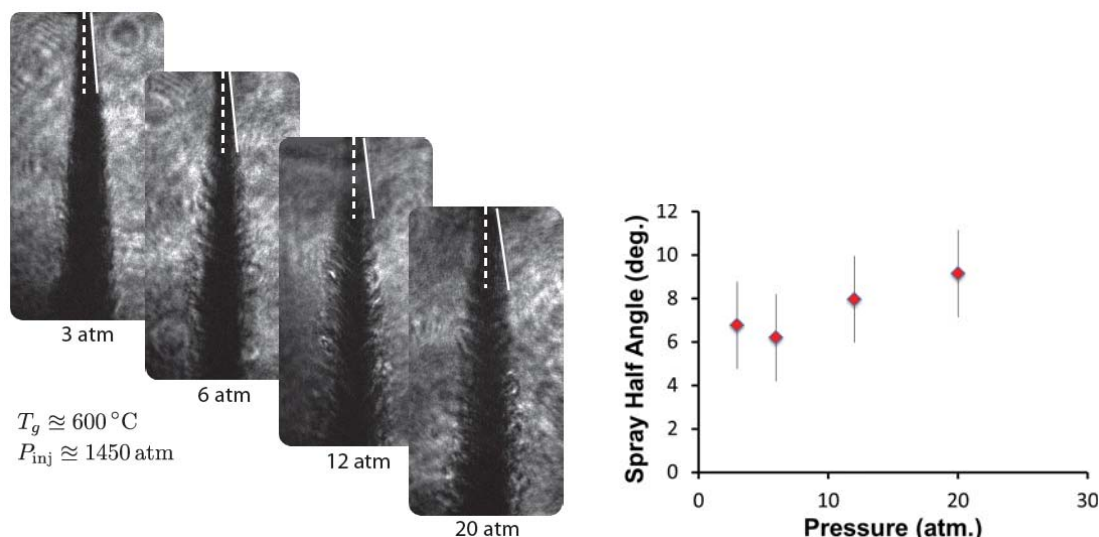


Figure 22: (left) Example images which exhibit the trend of increasing cone angle with pressure. (right) Averaged cone angle for all sprays studied. Data points are averages over ~30 images each. Error bars represent one standard deviation.

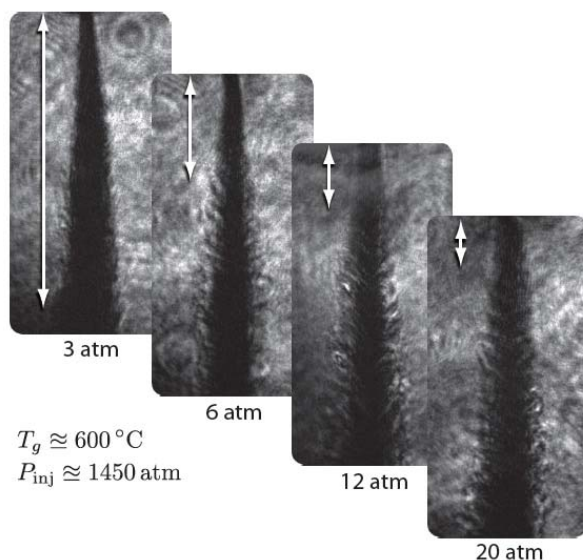


Figure 23: The offset distance between the shedding structures and the injector orifice varied with pressure.

A comparison of the spray cone angles of images taken at 20 atm and 25°C and those taken at 20 atm and 600°C reveal some interesting trends. Cone angle measurements were made of sprays over the entire injection event at the two aforementioned environmental conditions and plotted in Figure 24. The lower temperature spray reveals oscillation of the cone's angle, whereas the higher temperature spray initially oscillates but then settles to an almost constant angle. Interestingly, this temporal region corresponds directly with the existence of the shedding structures caused by violent mass shedding. A similar trend is observed at 12 atm and 600°C.

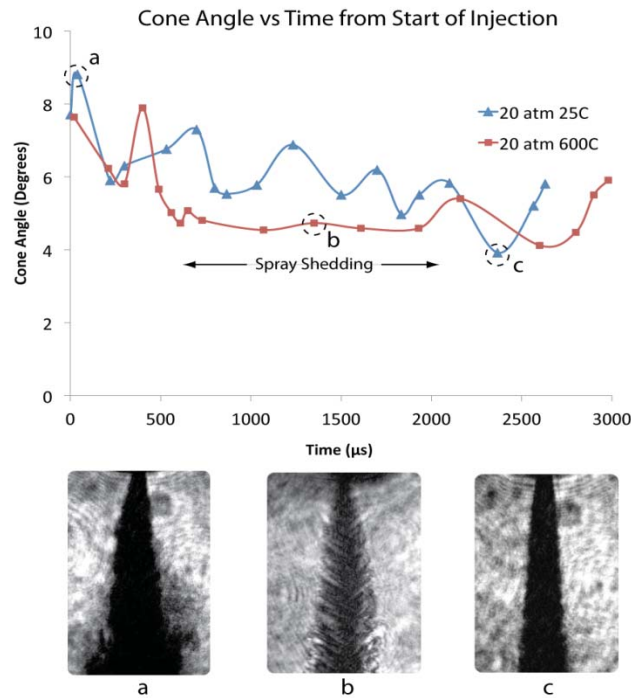


Figure 24: Measured spray cone angles as a function of time. Sprays were injected into a 20 atm environment at 25° and 600°C. The smooth region of the 600°C curve corresponds to the observation of spray shedding.

### 3.3.8 Spray structure in a biodiesel surrogate

To investigate the effect of fuel type on the near-nozzle region of diesel sprays, methyl oleate was substituted for dodecane for a series of images. Methyl oleate ( $C_{19}H_{36}O_2$ ) is a common surrogate for biodiesel. The resulting spray images were very clearly different than those of the low air temperature and pressure dodecane tests. Foremost, the spray cone was markedly wider in the methyl oleate images (Figure 25). Additionally, the images reveal what appear to be large shedding structures along the periphery. This scale of shedding is not observed in the ambient dodecane images, but has been observed in high temperature and pressure dodecane sprays as discussed. The reason for these shedding structures in methyl oleate is not understood. In fact the increased viscosity of methyl oleate relative to dodecane should inhibit breakup (Table 2). Further imaging of biodiesel surrogates is planned.

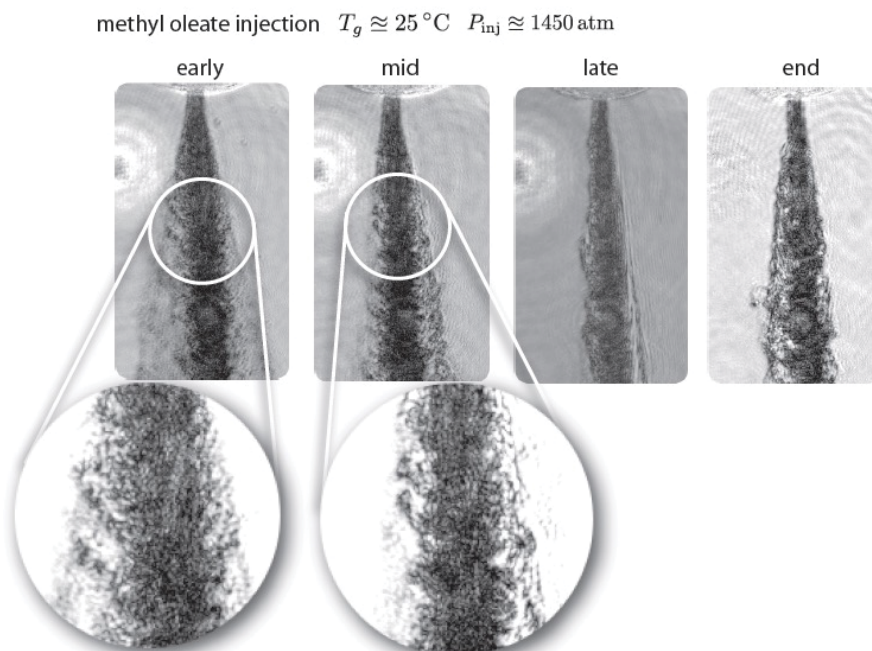


Figure 25: Images of methyl oleate reveal a wider spray cone and peripheral shedding.

### 3.4 Conclusions

The first successful demonstration of picosecond ballistic imaging of a diesel spray injected into high temperature and pressure air has been achieved. This technique has been applied to diesel injection sprays of dodecane and methyl oleate. Injection into ambient air reveals several trends in the near-nozzle region including oscillation in spray cone angle in time, fuel effects, and the impact of the injection pressure on spray cone angle. Ballistic images of dodecane sprays in an environment typical of diesel engines demonstrate marked trends of cone angle fluctuation and significant mass shedding. These shedding structures were not observed at room temperature operating conditions and are approximately described as having a spatial frequency of  $10\text{ mm}^{-1}$  with lengths of 50 to 200 microns. Structures imaged at high temperature and pressure bear resemblance to those predicted by the modeling community, and should help improve overall understanding of the underlying fluid dynamics. Images of methyl oleate at room ambient conditions reveal a spray that is wider and has a “richer” shedding structure than that observed at similar conditions with dodecane.

## 4 Two-Color Droplet Scattering

In order to probe the three-dimensional structure of diesel sprays, the ps laser pulse was converted to a laser sheet and passed through the spray for orthogonal imaging of the scattered light. These images were captured using the 532nm and 355nm output of the laser for two simultaneous images of the spray at different locations in the spray.

### 4.1 Introduction

Ballistic images, while able to probe dense regions of the spray, present 2-D path-averaged maps of light attenuation that obscure much of the internal structure of the spray. Diesel sprays are highly transient with significant variation in internal structure that requires volumetric imaging (3-D) techniques to capture the spray breakup physics. Using a thin ( $\sim 100\text{ }\mu\text{m}$ ) sheet to slice through the spray provides a 2-D map of spray internal structure that is not path averaged. By simultaneously imaging multiple sheets at different locations in the spray, we are able to extract



structure within the spray that is obscured by ballistic imaging techniques. These image sets are a first step toward fully three-dimensional imaging in diesel sprays.

Scattering images were collected at two injector orifice sizes (160  $\mu\text{m}$  and 320 $\mu\text{m}$ ), with two fuels (methyl oleate and dodecane), at increasing times after start of injection (ASOI), at offset distances from the injector line of center, and over a range of injector pressures (400 atm to 1450 atm).

## 4.2 Experimental Methods

Scattering measurements are based on the elastic interaction of a laser sheet with the liquid/gas spray field. As configured for this sequence of experiments, these measurements produce “spatially-resolved” measurements as opposed to the “line-integrated” measurements from the more traditional ballistic imaging methods. Spatial resolution comes from the intersection of the laser sheet with the perpendicular oriented object field provided by the camera. The size of each voxel or volume based resolution element is therefore the area of each pixel with the depth of the measurement defined by the width of the laser sheet. Thus, the camera provides image based resolution from the size of the camera’s imaging chip and the laser “slices” a section of the spray for interrogation by the camera.

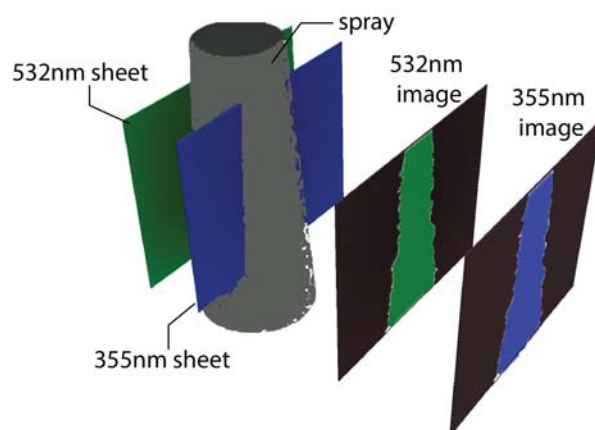


**Figure 26. Two-sheet scattering measurement.** 532nm and 355nm pulse sheets are simultaneously passed through the spray. Images of the scattering from these sheets is captured by two camera systems.

Figure 26 illustrates the basics of the measurement and shows two laser sheets, parallel to each other, but offset by a controlled distance, that are used to acquire spatially resolved images of the spray. A critical aspect of these experiments is the dual color laser sheets. Each experiment allows acquisition of an image pair that are at the same instant in time but, by controlling the offset in the sheets relative to one another, two simultaneous images of the spray are produced. This measurement is enabled by the distinct wavelengths of the two sheets (Nd:Yag second and third harmonic) which allows each camera to observe only the signal from the laser sheet assigned to the camera with the use of a band pass filter. Over a series of experiments, by varying the arrival time of the laser sheet in the spray, and then by controlling the spray position relative to the laser sheet, a time series of “volume images” can be created. Simultaneously acquired images can be correlated for similar structures in the spray field.

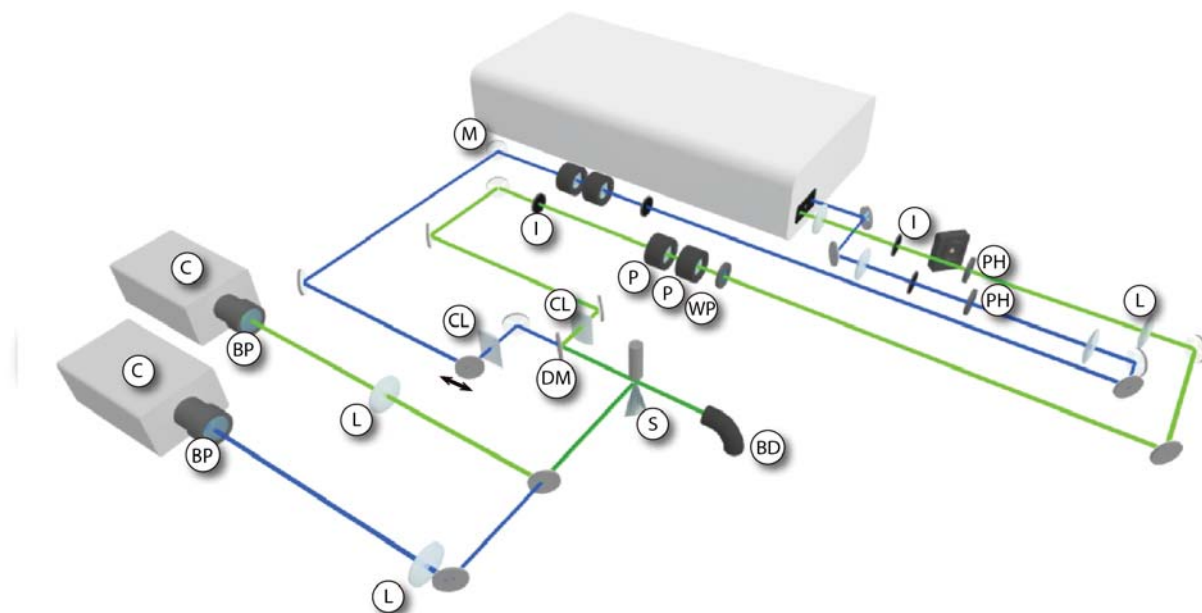


**Figure 27. Experimental setup for two-color scattering measurement. Green beam (532nm), blue beam (355nm), C: camera, L: lens, I: iris, PH: laser pinhole, P: polarizer, WP: wave plate, M: mirror, CL: cylindrical lens, DM: dichroic mirror, S: spray, BD: beam dump, BP: band pass filter.**

Figure 27 illustrates the overall experimental setup comprised of the Continuum Leopard, a series of beam shaping and delivery optics, the Sturman injector system which can be configured with spray nozzles with different hole sizes and orientations, scattering signal collection optics, and finally, the matched pair of Myo cameras.

The Continuum Leopard is one of the cornerstone pieces of equipment for this experimental program. This laser is intended to provide “turn-key” access to approximately 15 picosecond long pulses. The laser itself is one of the many lasers built around the properties of Nd:Yag and can be configured to provide multiple coincident beams that are fundamental in frequency (1.06 microns), second harmonic (532 nm), third harmonic (355 nm), or fourth harmonic (266 nm). Access to harmonics is provided by frequency doubling (or in the case of third harmonic, combined doubling and then frequency addition) crystals that are placed in the beam path after amplification. A critical element in using this laser feature is to note that the user must provide color separation of the beams since frequency shift crystals are not 100% efficient.

The beam pair exits the laser: one laser aperture for the 355 nm beam (this beam includes components of 532 nm and 1.06 microns as well) and the other aperture for 532 nm (this beam includes components of 1.06 microns as well). Use of dichroic reflectors for the 355 nm beam are used to direct the beam along on optical rail that includes focusing lenses, variable apertures, and laser pinholes. The dichroic reflector effectively removes the first and second harmonic from the beam. The 532 nm beam is similarly directed along an optical rail that includes focusing lenses, variable apertures, and a laser pinhole. Wavelength separation is both from the variable apertures (beam propagation direction and size for the fundamental wavelength beam is not exactly the same as for the second harmonic) and then dichroic reflectors at the end of the rail. Both beams are carefully “managed” with the use of a Keplerian telescope. This telescope combines two focusing lenses that are separated by the approximate sum of the two focal lengths. The size of the exiting beam is approximately equal to the entrance beam size times the ratio of the exiting focal length to the entrance focal length for the two lenses. These telescopes are critical to the experiment because: 1) they allow us to set the beam diameter, 2) the

telescopes can be arranged so that the midpoint of the Raleigh range for the beam is close to the exiting lens, and 3) a pinhole can be added to the focus plane for the telescope.

Setting the beam diameter, allows us to fix the size of the beam to the approximate height of the spray field to be imaged. Setting the beam waist close to the exiting telescope lens is important as well. The laser beams diverge, but within the so called “Raleigh range” the beam diameter is approximately constant. The length of the Raleigh range can be quite long with the length proportional to beam diameter (for instance, a 532nm beam with diameter of 8 mm has a Raleigh range of 0.378 m). While the Raleigh range can be comfortably long for this series of experiments so that the beam does not diverge appreciably, the beam waist can be located nearly anywhere along the beam path. Control of the lens separation provides control of the beam waist position, which then provides a non-divergent beam for the distances used in this experiment.

Finally, the use of a diamond pinhole at the focus plane is critical to the overall success of the experiment. A critical aspect of the experiment is using beam shaping optics to set the width of the laser sheet that traverses the spray. This sheet needs to be relatively small (of the order of 100 microns) in order to “slice” the spray into multiple discrete elements. While an exact Gaussian beam is not a requirement for beam focusing, strongly non-Gaussian beams simply will not produce aggressively small diameters. A pinhole at the focus plane for the Keplerian telescope can be used to reject the strongly non-Gaussian beam components with the results being a more “Gaussian-like” beam at the exit of the telescope. Because of the ultrafast nature of these measurements, instantaneous energy intensities at the focus plane are quite high and even diamond pinholes cannot withstand repeated impact from the laser fluence. Careful alignment of the beam at low power, along with out-of-focus larger pinholes used to provide some of the beam energy rejection required (not all of the apertures are shown in the diagram) allows the pinhole to reject energy along the edge of the beam while passing the very high intensity energy spot that represents the Gaussian components of the beam.

Following the exit from the Keplerian telescopes, the beams are directed back along the optical table and pass through waveplates (not required for 355nm) and polarizers to produce horizontal polarized light for both beams. Each beam is then directed through a cylindrical lens with the beams combined on green dichroic mirror (this mirror is fully transmissive to the 355 nm beam). The beams are carefully aligned to be parallel both by being exactly horizontal in terms of the sheet profile and parallel in their propagation both vertically and side-to-side horizontally. Beam position can be controlled using a translation stage on the 355 nm beam reflector; thus beam separation can be chosen and controlled. Typical beam profiles, created by sequentially traversing a razor blade across the beam and monitoring the beam energy after the laser blade with an energy meter, had beam widths of 149 $\mu$ m (fwhm) for 532 nm and 126  $\mu$ m (fwhm) for 355 nm.

Cameras are arranged to share a field of view with a green dichroic mirror used to “combine” the camera imaging paths. Each camera imaging path uses a relay lens to form an intermediate image. Subsequent to this image is the traditional camera lens that focuses the intermediate virtual image onto the camera imaging chip. Both imaging paths include a limiting aperture that can be measured. This allows us to set the collection angle for the scattering signal and is an important for calculating the signal strength. The camera lens for the 532 nm light is a Cannon MPE65 and has excellent macro capability allowing us to set the image size to the height desired. The lens for the 355 nm beam is a 105 mm UV Nikkor multi-element quartz lens specifically manufactured for use with UV signals. This lens is not intended for macro use and it was important to use the relay lens to magnify the image. Because of the UV light in this signal,

a fused silica lens pair (plano convex with the curved elements facing each other) was used to enhance optical performance beyond the capabilities of a single element lens. For the green beam path, a commonly available visible wavelength achromat was used.

Beam energy for each of the beams was determined at the start and/or end of each experimental series and was based on a 100 shot average of beam energy. Typical energies delivered to the image plane were  $150 \pm 6 \mu\text{J}$  (355nm) and  $1.25 \pm 0.09 \text{ mJ}$  (532nm).

### 4.3 Results

The following series of figures capture highlights from the sprays that were investigated. As noted in the previous section, data was acquired for various planes of the spray field with the Sturman injector that has been used elsewhere in this work. Injection pressures were (unless otherwise noted) 1450 atm into an ambient pressure and temperature background environment. Future experiments, if possible, would use the high pressure and temperature spray facility to capture images at diesel relevant conditions. The injection system was used with two fuels, dodecane and methyl oleate and two orifice sizes, 160 and then 320 microns diameter. These orifices were custom machined into blank Bosch nozzle tips and then flow tested at conditions very similar to those used for the experiments. These four experiments formed the basis for our current imaging data set that is comprised by over 3000 images. This section begins the examination of this data and what it can tell us about the spray.

Figure 28 shows images from the approximate centerline of the spray with the laser propagating from right to left in all of the images (and this is the consistent presentation with all of the scattering images in this report). The first three images (left side) are different images for the exact same condition: 0.6 ms after the start of injection for the same section of the spray with a 320 micron injector tip. Worthy of note is the highly defined spray exit right at the injector tip. Observable effects of laser attenuation as it traverses the spray are not present. For these images, it is also noteworthy that the interior of the spray includes significant structure with significant signal level increases on the left side of the spray. This indicates non uniform fuel loading of the spray plume for this planar slice of the spray. Both interior structures and the distinct spray plume interface with the surrounding environment are consistent with vigorous mixing; these structures are similar to those observed in shear layers that are mixing two fluid streams. The images are also not consistent with a spray structure that has dominant liquid only regions. Neither at the spray tip, nor in other spray regions is there evidence of extended fluid structures. The spray is instead consistent with a fully atomized spray as the fuel leaves the injector tip. Presumably cavitation in the nozzle provides for pre-exit breakup. The jet itself appears to be a high droplet volume fraction fluid region exiting into the ambient environment. Hence the mixing is between a high droplet volume fraction, high velocity jet with the surrounding ambient region. Mixing structures in these images are of length scales of 1 mm and below and are present both at the exterior of the jet and also show significant structures within the jet itself.

The fourth image is an average of the three left most images. This average shows two distinct things. First, the average is close enough to the original images that it illustrates the experiments are very repeatable. Observed cone angle and the sorts of structure are repeatable as are the relative position of the high fuel bearing regions of the spray. Second, the average image shows much less detail in terms of mixing structure in the spray. The fine scale mixing structures are not as present in the average image. This motivates both the need to capture instantaneous images and also shows the role of acquisition time on the image. Methods that integrate over a



time period even as short as 100 picoseconds will “blur” the mixing structures shown in this image.

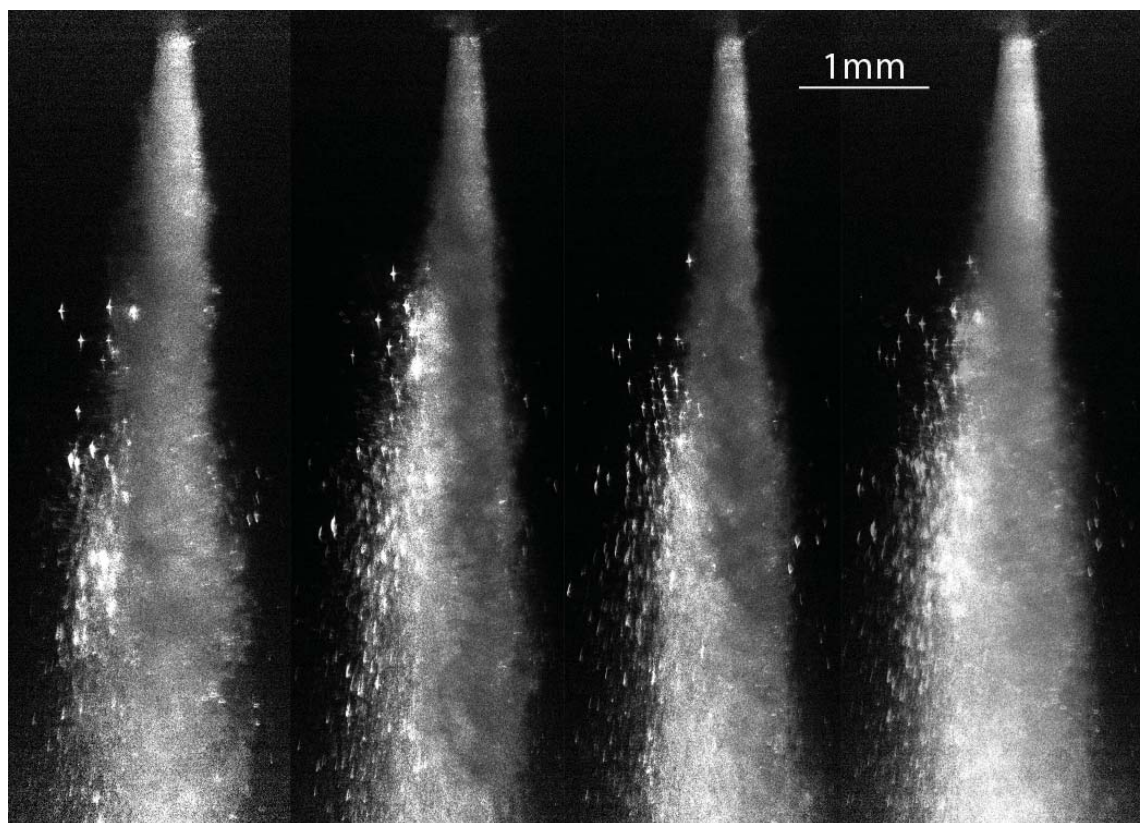


Figure 28. Dodecane spray (320  $\mu\text{m}$  injector) at 0.6 ms ASOI.

Figure 29 illustrates a fine-scale walk through the spray centerline for a dodecane spray through a 160 micron orifice. For more than a decade, spray researchers have speculated on the existence of a spray core. Within these images, we see no evidence of a spray core. As with Figure 28, all images are consistent with fully atomized spray as it exits the nozzle. Also as with the prior image set, the mixing of the high fuel bearing jet includes fine scale structures and the interior of the jet is not homogeneous.

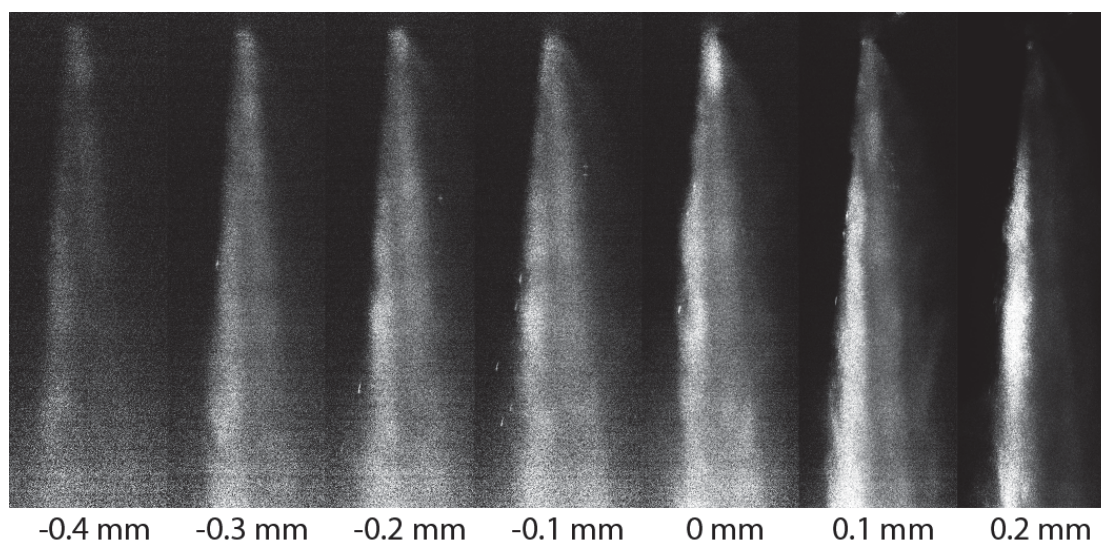


Figure 29. Scattering images of dodecane injections at 1.9 ms ASOI. Spray position moved relative to beam. Dimensions listed are offset from spray centerline, with negative values being further from the camera.

Figure 30 illustrates end of spray behavior for both fuels through both orifices. It also includes an image that has an oil ligament added to show what an intact core would look like. All four images show significant structure and the 320 micron images seem to have a long wavy structure that could be contiguous fluid. However, we do not observe the intact core that has been discussed that tapers to a point over ten or twenty diameters from the jet exit.

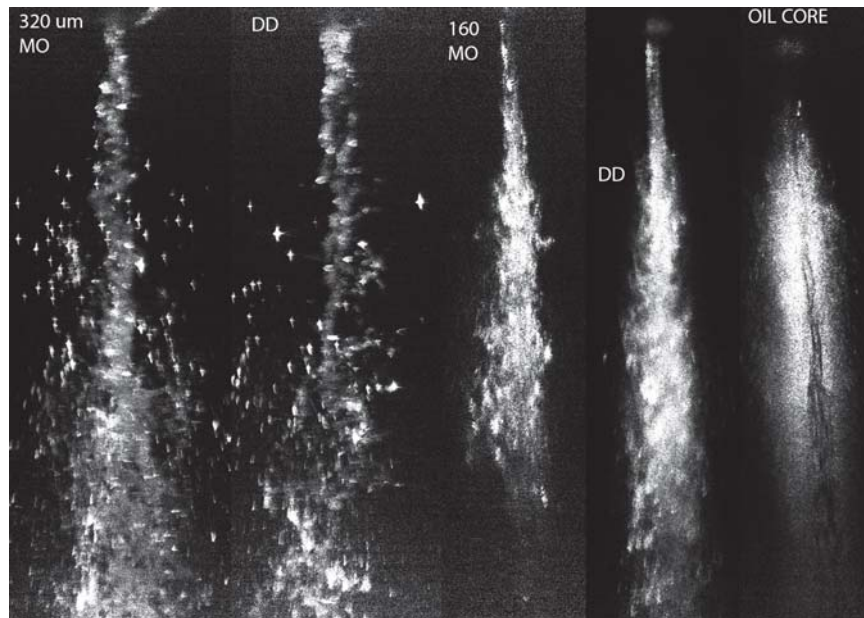


Figure 30. End of spray images (355 nm) showing effect of fuel type and orifice size. Oil was added to the tip of the injector to simulate what a liquid core would look like.

Figure 31 continues the experimental search for a spray core by slicing the spray on centerline and then lowering the injection pressure for successive spray events. All of the sprays show significant interior structures and these structures become more significant as the injection pressure falls. However, we still do not observe an intact fluid region immediately adjacent to the jet orifice.

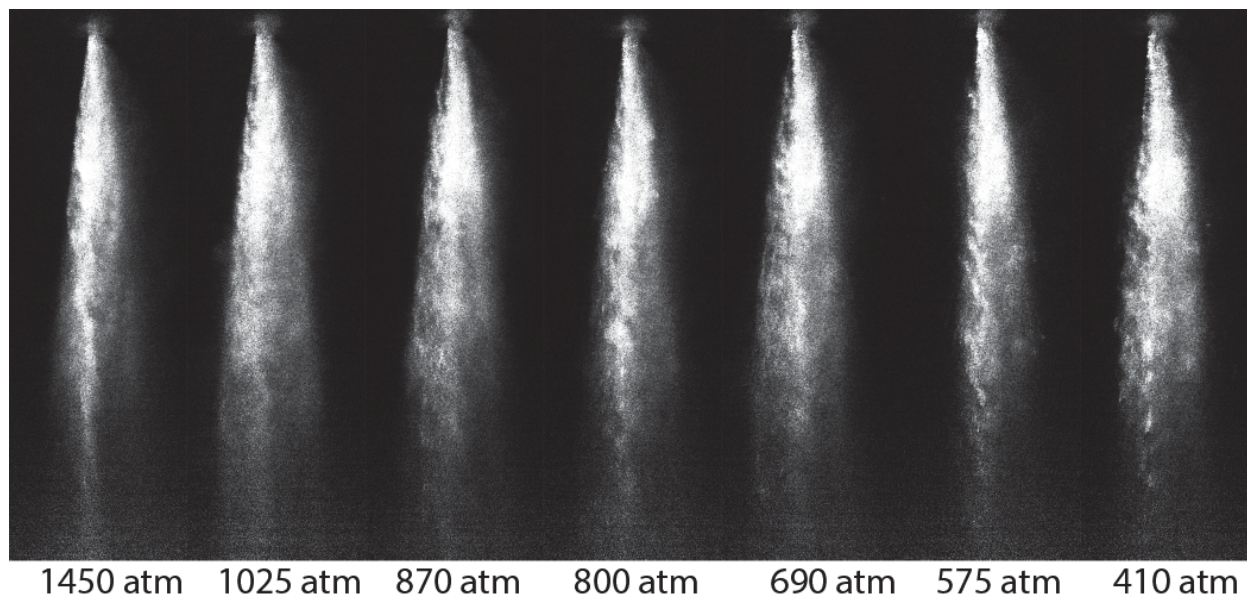


Figure 31. On centerline images of dodecane spray (160  $\mu\text{m}$  injector) with decreasing injection pressure.

Figure 32 continues the comparison between fuels and orifice sizes. These results are for 0.3 ms after injection approximately on the centerline. The result for methyl oleate with a 320 micron



injector is especially striking. Recall that for the line-integrated images, we had observed significant “thread-like” structures at nearly all injection conditions. What we see in the first two images is a dramatic difference in the break up behavior for methyl oleate and dodecane. While both sprays are significantly “structured” in the spray interior, the methyl oleate is clearly not breaking up as well and appears to have larger variation in the local volume fraction of the fuel. The 320 micron hole dodecane data is interesting in its own right as it shows a nearly empty central region surrounded by two high fuel bearing regions immediately downstream of the orifice. Structures at the edge of this spray clearly show that it is shedding mass with eddy like structures on the edges of both sides of the spray. The 160 micron data has finer-scale mixing structures at the spray edge and the interior structures are not as dramatic. However, the dodecane spray shows a strong asymmetry in fuel loading with the left side of the spray clearly holding the majority of the fuel in the system. Again, this image set emphasizes the strong mixing of the jet as it moves downstream and the equally strong inhomogeneity in the fuel loading of the jet itself.

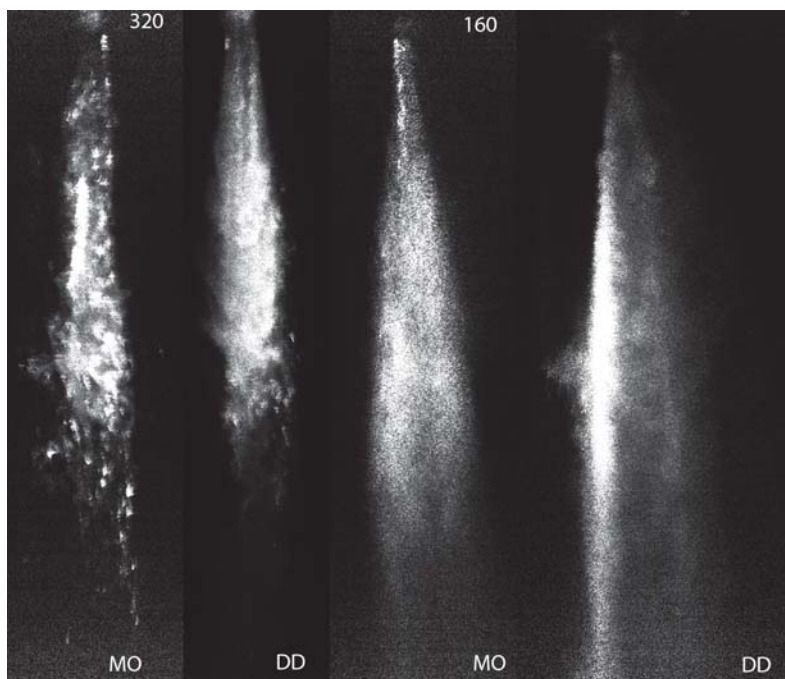
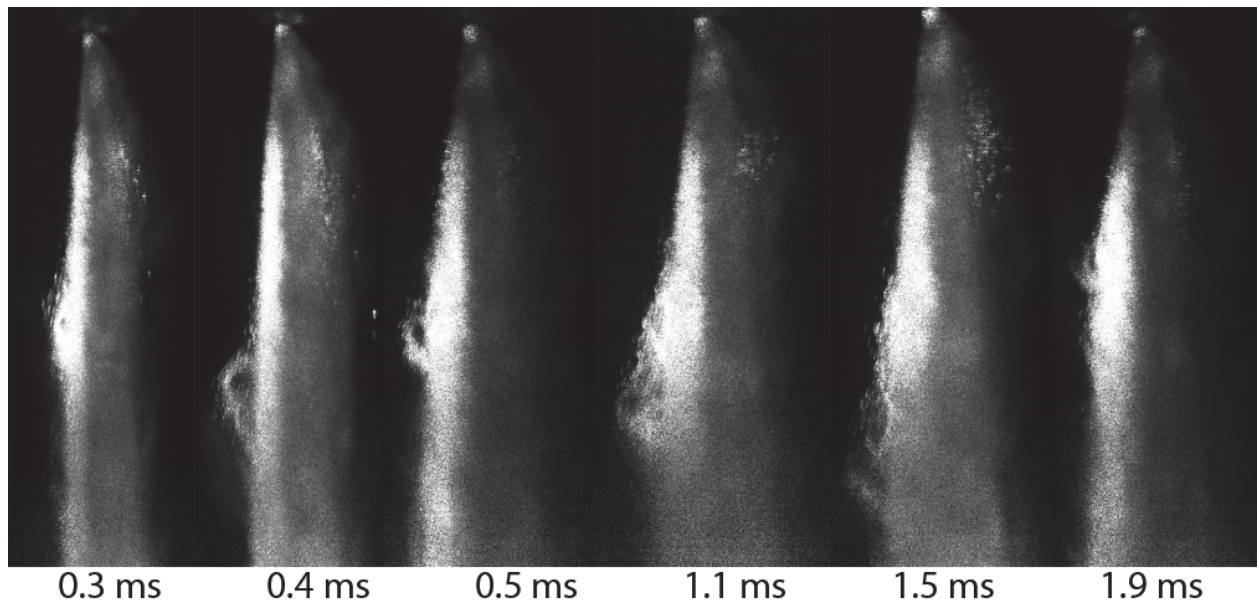


Figure 32. 355nm image of spray at 0.3 ms ASOI. Typical spray features due to fuel effects and orifice size differences.

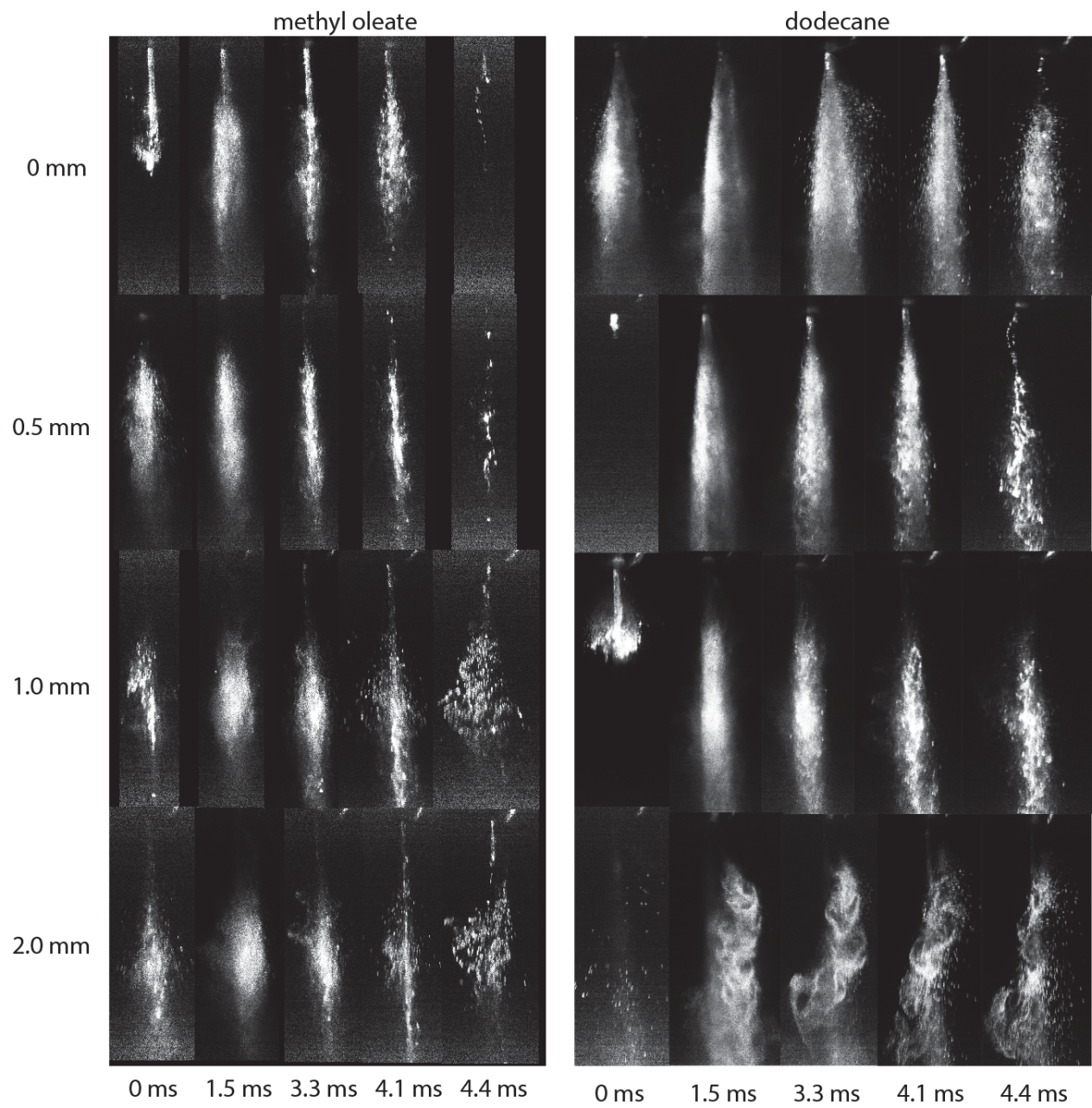
Figure 33 shows a time series for the jet with dodecane as the fuel and the orifice of 160 microns. This figure shows a consistent set of shedding structures on the left side of the image. This is not an image of the progression of the same structure because of the span of time for these images. Clearly, the spray produces consistent eddies on the left side of the spray. This is the same side as the heavily fuel laden part of the spray, noting that the high fuel loading on the left side is consistently observed at all times.



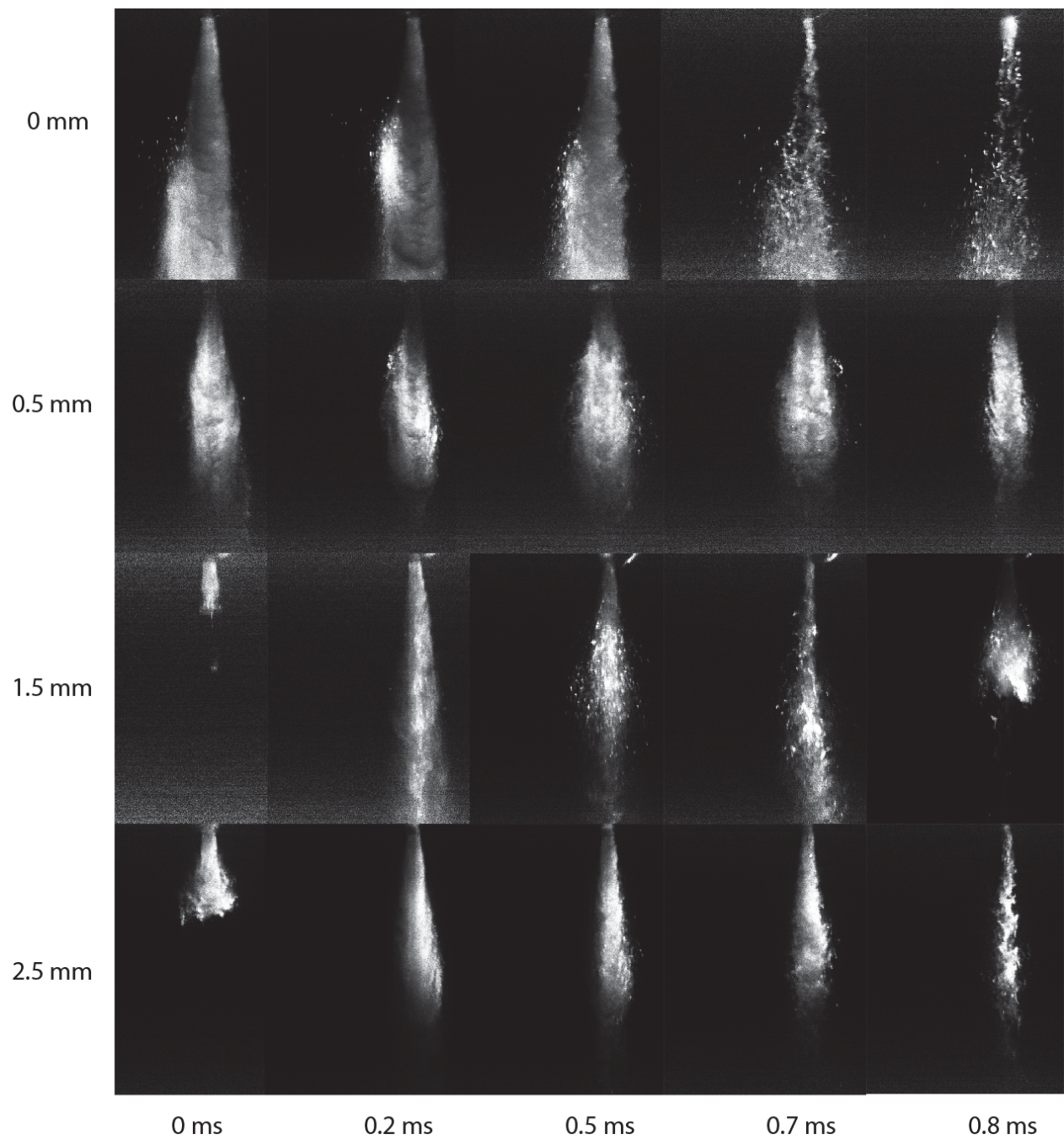
**Figure 33. Dodecane injection, 160  $\mu\text{m}$  injector, with 355nm laser. Droplet vortices are present in the spray.**

Figure 34 through Figure 36 illustrate the power of this technique. Within these image panels, time and spatial structure are captured. Notable effects in these images are: the strong difference in edge structures for dodecane and methyl oleate. The methyl oleate is clearly more prone to coming apart in “chunks” which is consistent with the observations of the line integrated images. The dodecane seems to produce more of highly structured sprays, but with a more diffuse cloud on the spray edge. This difference in fuel behavior continues to be present in the larger orifice sprays. Dodecane appears to atomize more fully compared to methyl oleate, which appears to create structures that are larger in scale.





**Figure 34.** Methyl oleate (left) and dodecane (right) injected from 160  $\mu\text{m}$  orifice at 1450 atm (imaged with 355 nm wavelength).



**Figure 35.** Dodecane injected from 320  $\mu\text{m}$  orifice at 1450 atm (imaged with 355 nm wavelength).



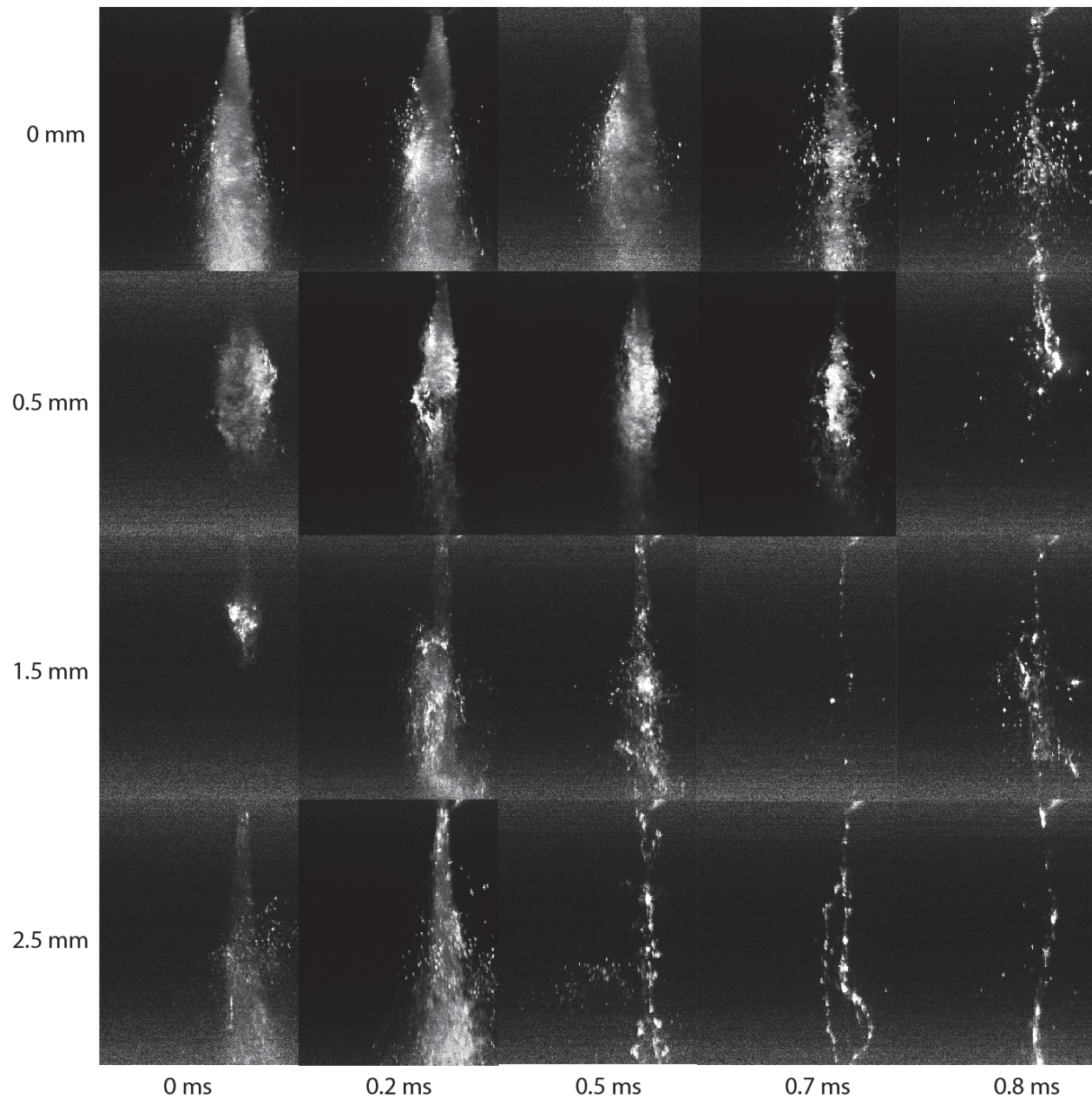


Figure 36. Methyl oleate injected from 320  $\mu\text{m}$  orifice at 1450 atm (imaged with 355 nm wavelength).

## 4.2 Conclusions

We have demonstrated high-resolution ( $< 10 \mu\text{m}$ ) instantaneous ( $< 15 \text{ ps}$ ) laser sheet scattering imaging of diesel sprays. Images reveal that contrary to conventional thinking, the attenuation of the laser sheet is not sufficient to preclude complete two-dimensional cross sections of the spray. Further, a careful traversing of the spray through the laser sheet finds no evidence of an intact liquid core, even at low injection pressures. The spray appears to be a largely atomized droplet-laden flow exhibiting shear-driven vortices. Further, the optical depth of the spray allows for embedded spray structures to be successfully imaged from orthogonal images of laser sheets.

## 5 Project Summary

The objectives of this project were to develop advanced imaging techniques to improve understanding of breakup phenomenon in the near-nozzle region of high injection pressure diesel sprays. Several advanced optical techniques have been developed, including:

- the first demonstration of picosecond ballistic imaging in diesel sprays
- the first ballistic imaging of diesel sprays at elevated temperature and pressure
- the first direct and simultaneous comparison of ballistic and shadowgraphy imaging of diesel sprays
- and the first demonstration of short-pulse, multi-wavelength laser sheet scattering imaging in diesel sprays.

These diagnostics have been applied to diesel sprays revealing the following improved understanding of spray behavior:

- there is significant variation in spray structure with fuel type (dodecane and methyl oleate)
- dramatic shearing of droplet laden flow is observed at high pressure and temperature
- there is a significant reduction in optical depth at elevated temperature and pressure
- there is no evidence of a liquid core, even at low injection pressures

The observation that a picosecond laser sheet can in fact penetrate the near-nozzle diesel spray motivates future efforts to advance volumetric imaging of these sprays and extend this effort to high temperature and pressure, where optical depth is even less. Continued development of multispectral imaging techniques that produce multiple cross sections of the spray at a given instant will reveal the three-dimensional structure of diesel sprays needed to improve injection models leading to gains in fuel efficiency.

## 6 References

- [1] M. Herrmann, "On simulating primary atomization," *At. Sprays*, vol. 23, no. 11, pp. v–ix, 2013.
- [2] O. Desjardins, J. McCaslin, M. Owkes, and P. Brady, "Direct numerical and large-eddy simulation of primary atomization in complex geometries," *At. Sprays*, vol. 23, no. 11, pp. 1001–1048, 2013.
- [3] N. Chigier, W. Bachalo, R. D. Reitz, J. Bellan, and M. Herrmann, "Spray control for maximizing energy efficiency and reducing emission in combustion engines," *At. Sprays*, vol. 21, no. 7, pp. 553–574, 2011.
- [4] D. Jarrahbashi and W. A. Sirignano, "Acceleration Effects on Instability of High-Pressure Fuel Jets," in *Proceedings of the Twelfth International Conference on Liquid Atomisation and Spray Systems (ICLASS)*, Heidelberg, Germany, 2012.
- [5] D. Jarrahbashi and W. A. Sirignano, "Vorticity dynamics for transient high-pressure liquid injection," *Phys. Fluids*, vol. In Press.
- [6] S. Duran, J. M. Porter, and T. R. Parker, "Ballistic Imaging of Sprays at Diesel Relevant Conditions," in *Proceedings of the Twelfth International Conference on Liquid Atomisation and Spray Systems (ICLASS)*, Heidelberg, Germany, 2012.

- [7] T. E. Parker, L. R. Rainaldi, and W. T. Rawlins, "A comparative study of room-temperature and combusting fuel sprays near the injector tip using infrared laser diagnostics," *At. Sprays*, vol. 8, no. 5, p. 565, 1998.
- [8] J. Shinjo and A. Umemura, "Simulation of liquid jet primary breakup: Dynamics of ligament and droplet formation," *Int. J. Multiph. Flow*, vol. 36, no. 7, pp. 513–532, Jul. 2010.
- [9] W. D. Bachalo and M. J. Houser, "Phase/Doppler spray analyzer for simultaneous measurements of drop size and velocity distributions," *Opt. Eng.*, vol. 23, no. 5, pp. 583–590, 1984.
- [10] S. V. Sankar, B. J. Weber, D. Y. Kamemoto, and W. D. Bachalo, "Sizing fine particles with the phase Doppler interferometric technique," *Appl. Opt.*, vol. 30, no. 33, pp. 4914–4920, Nov. 1991.
- [11] G. A. Ruff, L. P. Bernal, and G. M. Faeth, "Structure of the near-injector region of non-evaporating pressure-atomized sprays," in *27th AIAA Aerospace Sciences Meeting*, 1989, vol. 1.
- [12] L. Arnone, F. Beretta, A. Tregrossi, A. D'Alessio, and F. Ossler, "Ensemble and time resolved light scattering measurements in isothermal and burning heavy oil sprays," *Symp. Int. Combust.*, vol. 24, no. 1, pp. 1549–1555, 1992.
- [13] F. Beretta, A. Cavaliere, and A. D'Alessio, "Ensemble laser light scattering diagnostics for the study of fuel sprays in isothermal and burning conditions," *Symp. Int. Combust.*, vol. 20, no. 1, pp. 1249–1258, 1985.
- [14] L. G. Dodge, D. J. Rhodes, and R. D. Reitz, "Drop-size measurement techniques for sprays: comparison of Malvern laser-diffraction and Aerometrics phase/Doppler," *Appl. Opt.*, vol. 26, no. 11, pp. 2144–2154, Jun. 1987.
- [15] P. G. Felton, A. A. Hamidi, and A. K. Aigal, "Measurement of drop size distribution in dense sprays by laser diffraction," in *Proceedings of the Third International Conference on Liquid Atomisation and Spray Systems (ICLASS)*, London, England, 1985, vol. 2.
- [16] Y. Yue, C. F. Powell, R. Poola, and J. Wang, "Quantitative measurements of diesel fuel spray characteristics in the near-nozzle region by using x-ray absorption," *At. Sprays*, vol. 11, no. 4, pp. 471–490, 2001.
- [17] Z. Liu, K. S. Im, X. Xie, Y. Wang, X. Zhang, S. Moon, J. Gao, K. Fezzaa, M. C. Lai, K. Harkay, and others, "Ultra-Fast Phase-Contrast X-ray Imaging of Near-Nozzle Velocity Field of High-Speed Diesel Fuel Sprays," *ILASS-Am. Cincinnati Ohio USA*, 2010.
- [18] W.-K. Lee, K. Fezzaa, and J. Wang, "Metrology of steel micronozzles using x-ray propagation-based phase-enhanced microimaging," *Appl. Phys. Lett.*, vol. 87, no. 8, p. 084105, 2005.



- [19] M. Linne, “Analysis of X-ray phase contrast imaging in atomizing sprays,” *Exp. Fluids*, vol. 52, no. 5, pp. 1201–1218, 2012.
- [20] M. Linne, “Imaging in the optically dense regions of a spray: A review of developing techniques,” *Prog. Energy Combust. Sci.*, vol. 39, no. 5, pp. 403–440, Oct. 2013.
- [21] P. F. Flynn, R. P. Durrett, G. L. Hunter, O. C. Akinyemi, J. E. Dec, and C. K. Westbrook, “Diesel Combustion: An Integrated View Combining Laser Diagnostics, Chemical Kinetics, And Empirical Validation,” 1999.
- [22] M. Paciaroni, M. Linne, T. Hall, J. P. Delplanque, and T. Parker, “Single-shot two-dimensional ballistic imaging of the liquid core in an atomizing spray,” *At. Sprays*, vol. 16, no. 1, pp. 51–70, 2006.
- [23] M. Paciaroni and M. Linne, “Single-Shot, Two-Dimensional Ballistic Imaging through Scattering Media,” *Appl. Opt.*, vol. 43, no. 26, pp. 5100–5109, 2004.
- [24] M. Linne, M. Paciaroni, T. Hall, and T. Parker, “Ballistic imaging of the near field in a diesel spray,” *Exp. Fluids*, vol. 40, no. 6, pp. 836–846, Feb. 2006.
- [25] Z. Falgout, M. Rahm, Z. Wang, and M. Linne, “Evidence for supercritical mixing layers in the ECN Spray A,” *Proc. Combust. Inst.*, vol. 35, no. 2, pp. 1579–1586, 2015.
- [26] L. WANG, P. P. HO, C. LIU, G. ZHANG, and R. R. ALFANO, “Ballistic 2-D Imaging Through Scattering Walls Using an Ultrafast Optical Kerr Gate,” *Science*, vol. 253, no. 5021, pp. 769–771, 1991.
- [27] H. Purwar, S. Idlahcen, C. Rozé, D. Sedarsky, and J.-B. Blaisot, “Collinear, two-color optical Kerr effect shutter for ultrafast time-resolved imaging,” *Opt. Express*, vol. 22, no. 13, pp. 15778–15790, Jun. 2014.
- [28] S. Idlahcen, L. Méès, C. Rozé, T. Girasole, and J.-B. Blaisot, “Time gate, optical layout, and wavelength effects on ballistic imaging,” *J. Opt. Soc. Am. A*, vol. 26, no. 9, pp. 1995–2004, Sep. 2009.
- [29] M. E. Paciaroni, “Time-gated ballistic imaging through scattering media with applications to liquid spray combustion,” Colorado School of Mines, Golden, CO, 2004.
- [30] F. Mathieu, M. A. Reddemann, J. Palmer, and R. Kneer, “Time-gated ballistic imaging using a large aperture switching beam,” *Opt. Express*, vol. 22, no. 6, p. 7058, Mar. 2014.
- [31] E. Berrocal, D. L. Sedarsky, M. E. Paciaroni, I. V. Meglinski, and M. A. Linne, “Laser light scattering in turbid media Part II: Spatial and temporal analysis of individual scattering orders via Monte Carlo simulation,” *Opt. Express*, vol. 17, no. 16, pp. 13792–13809, 2009.
- [32] N. Pfeiffer, P. Chan, G. H. Chapman, F. Vasefi, and B. Kaminska, “Optical imaging of structures within highly scattering material using a lens and aperture to form a spatiofrequency filter,” 2008, vol. 6854, p. 68541D–68541D–12.



- [33] W. Hentschel, “Modern tools for diesel engine combustion investigation,” *Symp. Int. Combust.*, vol. 26, no. 2, pp. 2503–2515, 1996.
- [34] M. K. Khair, “Progress in diesel engine emissions control,” *J. Eng. Gas Turbines Power*, vol. 114, p. 568, 1992.
- [35] J. B. Heywood, *Internal combustion engine fundamentals*. McGraw-Hill, 1988.
- [36] D. Nehmer, “personal communication,” Sturman Industries-2002.
- [37] D. L. Siebers, “Scaling liquid-phase fuel penetration in diesel sprays based on mixing-limited vaporization,” *SAE Tech. Pap.*, pp. 01–0528, 1999.
- [38] V. Diky, R. D. Chirico, C. D. Muzny, A. F. Kazakov, K. Kroenlein, J. W. Magee, I. Abdulagatov, J. W. Kang, and M. Frenkel, “ThermoData Engine (TDE) Software Implementation of the Dynamic Data Evaluation Concept. 7. Ternary Mixtures,” *J. Chem. Inf. Model.*, vol. 52, no. 1, pp. 260–276, Jan. 2012.
- [39] J. J. Jasper, “The Surface Tension of Pure Liquid Compounds,” *J. Phys. Chem. Ref. Data*, vol. 1, no. 4, pp. 841–1010, Oct. 1972.
- [40] K. M. Doll, B. R. Moser, and S. Z. Erhan, “Surface Tension Studies of Alkyl Esters and Epoxidized Alkyl Esters Relevant to Oleochemically Based Fuel Additives<sup>†</sup>,” *Energy Fuels*, vol. 21, no. 5, pp. 3044–3048, Sep. 2007.
- [41] W. A. Sirignano, *Fluid Dynamics and Transport of Droplets and Sprays*. Cambridge University Press, 1999.
- [42] S. P. Duran, J. M. Porter, and T. E. Parker, “Ballistic Imaging of Diesel Sprays Using a Picosecond Laser: Characterization and Demonstration,” *Appl. Opt.*, Under Review.
- [43] Z. Han, A. Uludogan, G. J. Hampson, and R. D. Reitz, “Mechanism of Soot and NO<sub>x</sub> Emission Reduction Using Multiple-injection in a Diesel Engine,” SAE International, Warrendale, PA, 960633, Feb. 1996.